ADVANCED MATERIALS INTERFACES
Open Access
www.advmatinterfaces.de

Surface Deposition Induced Reduction of the Ground State Spin in Cr_{10} Wheel

Elena Bartolomé, Ludovica Ferrari, Francesco Sedona, Ana Arauzo, Javier Rubín,* Javier Luzón, Julia Herrero-Albillos, Mirco Panighel, Aitor Mugarza, Marzio Rancan, Mauro Sambi, Lidia Armelao, Juan Bartolomé, and Fernando Bartolomé**

We report the deposition of monolayers and multilayers of $\{Cr_{10}(OMe)_{20}(O_2CCMe_3)_{10}\}$ wheels, hereafter $\{Cr_{10}\}$, onto Au(111) and Cu(111) single-crystal substrates, and their characterization combining scanning tunneling microscopy, X-ray photoelectron spectroscopy, X-ray absorption spectroscopy, X-ray natural linear dichroism, and X-ray magnetic circular dichroism (XMCD). $\{Cr_{10}\}$ in bulk shows axial magnetic anisotropy and a cluster total spin $S = 9$ ground state, stemming from an interaction scheme of two semi-crowns containing four Cr^{3+} ions interacting ferromagnetically, separated by two Cr^{3+} antiferromagnetically coupled. The one-monolayer (1ML) samples of $\{Cr_{10}\}$ sublimated on Ag(111) and Cu(111) show slightly different applied magnetic field dependence of XMCD signal. The field-dependence of the magnetization evolves from a lower curve for the 1ML $\{Cr_{10}\}$ samples to a curve resembling the bulk one as the number of layers is increased, as shown in a 14ML sample. Monte Carlo simulations allow rationalizing the magnetization curves of the 1ML samples in terms of a reduction of the cluster ground-state total spin, $S = 3$ or $S = 6$, as a consequence of variations in the intra-wheel coupling interactions induced by the on-surface deposition. The sensitivity of the magnetic configuration of $\{Cr_{10}\}$ to minor distortions of the intramolecular conformation might be exploited to control magnetism by external stimuli for applications.

1. Introduction

Efforts to assemble molecular magnets into layers of variable thickness have been fueled by the goal of developing low-dimensional magnetic materials with molecularly controllable properties, with interest in different fields, such as molecular spintronics or quantum computing, among others.[1] Molecules exhibiting magnetic hysteresis, known as single molecule magnets (SMMs),[2,3,4] have been intensively investigated, as they represent the ultimate miniaturization limit of magnetic memories and exhibit a rich quantum behavior.[5] The combination of a large spin of the molecule with an easy-axis magnetic anisotropy results in an energy barrier for the reversal of the magnetization. Accurate control of anisotropy by chemical design has led in recent years to 4f-based mononuclear SMMs[6,7] with energy barriers of ≈2000 K[8] at blocking temperatures as high as 80 K.[9,10] However, a necessary step to fully exploit the

E. Bartolomé
Escola Universitària Salesiana de Sarrià (EUSS)
Passeig Sant Joan Bosco 74, Barcelona 08017, Spain
E-mail: ebartolome@euss.es

L. Ferrari, F. Sedona, M. Sambi, L. Armelao
Dipartimento di Scienze Chimiche
Università di Padova
Via Marzolo 1, Padova 35131, Italy

A. Arauzo, J. Rubín, J. Herrero-Albillos, J. Bartolomé, F. Bartolomé
Instituto de Nanociencia y Materiales de Aragón (INMA)
Universidad de Zaragoza – CSIC
Pedro Cerbuna 12, Zaragoza 50009, Spain
E-mail: jrubin@unizar.es; bartolom@unizar.es

A. Arauzo, J. Bartolomé, F. Bartolomé
Departamento de Física de la Materia Condensada
Universidad de Zaragoza
Pedro Cerbuna 12, Zaragoza 50009, Spain

J. Rubín, J. Herrero-Albillos
Departamento de Ciencia y Tecnología de Materiales y Fluidos
Escuela de Ingeniería y Arquitectura
Universidad de Zaragoza
María de Luna 3, Zaragoza 50018, Spain

J. Luzón
Centro Universitario de la Defensa
Academia General Militar
Zaragoza Spain

The ORCID identification number(s) for the author(s) of this article can be found under https://doi.org/10.1002/admi.202300146

DOI: 10.1002/admi.202300146

functionalities of SMMs to store and process information is to find ways to deposit monolayers of organized molecules, individually addressable, onto suitable substrates.[11]

This challenging goal has stimulated the research of chemically stable molecules that withstand surface-deposition methods. The self-assembly of monometallic molecules, such as phthalocyanines,[12,13] porphyrins[14] and bis(phthalocyaninato) lanthanide-based complexes[15,16] is already well established, whereas there are only a few examples of polymetallic molecules robust enough to sustain a wide range of processes and experiments on surfaces, for example, $\{Fe_4\}$,[17] $\{Mn_6\}$,[18] and $\{Cr_7Ni\}$.[19] Deposition by sublimation in ultrahigh vacuum (UHV) is the cleanest method to prepare molecular overlayers, something highly important for experiments that are sensitive to the molecule-surface interaction. However due to the fragility of polymetallic complexes, sublimation has been only successfully demonstrated in a limited number of cases,[19–21] while liquid phase deposition methods have been predominantly utilized.

Understanding how the magnetic properties of molecular magnets are affected when supported on a substrate is crucial for their successful integration into solid-state devices. In archetypical $TbPc_2$, direct interaction with metallic substrate was observed to significantly impact the magnetic properties, and consequently, various strategies were proposed to avoid the loss of magnetic bistability, including the use of insulating decoupling layers,[22] conductive graphene/SiC(0001) substrates,[23] thicker films,[24] or spacers to graft the molecules to the substrates.[25,26] Recently, an extension of the lanthanide-driven SMM approach consisting on surface-supported periodic networks containing lanthanides has been proposed,[27] although SMM behavior has not been demonstrated yet.

An alternative approach to achieving robust on-surface SMMs has been through the use of endohedral metallofullerenes,[28,29] in which a pair of lanthanides with strong single-ion anisotropy and exchange coupling are encapsulated within a carbon cage. The high thermal stability of fullerenes enabled the formation of monolayers by sublimation both on metals and insulators.[30] Monolayers of functionalized fullerene $Tb_2@C_{80}(CH_2Ph)$ on graphene from solution displayed magnetic bistability up to a temperature of 28 K, which is the highest hysteresis temperature observed among air-stable SMMs.[31]

As regards polynuclear 3d-clusters, early attempts to demonstrate slow magnetic relaxation in Mn_{12} adsorbates on gold were unsuccessful owing to redox and structural rearrangement phenomena,[32] and even surface layers of bulk Mn_{12} exhibited no magnetic hysteresis, likely due to structural deformations.[33] The first demonstration of SMM behavior retention on surface was achieved for a sublimated monolayer of sulfur-functionalized $\{Fe_4\}$ cluster grafted on Au(111) at sub-kelvin temperatures.[34] The chemical stability and ease of functionalization of the $\{Fe_4\}$ family have been exploited to control their interaction with various substrates.[35,36] These propeller-like tetrairon(III) structures possess a cluster $S = 5$ ground state and anisotropy values of $D/k_B = -0.30$ to -0.65 K, resulting in energy barriers amounting to $U/k_B = 7.6 - 16.2$ K.[37] The introduction of anchoring insulating spacers[38] may difficult the integration in devices given the non-planar molecular geometry.

In this respect, the planar and highly symmetric structure of cyclic molecules makes them potentially suitable for deposition onto substrates.[20,39] Molecular cyclic complexes have received special attention owing to their interesting intrinsic magnetic properties, as model systems for the study of macroscopic quantum coherent phenomena, and their potential application as elementary units in high-density information storage and processing.[40–42] Magnetic wheels of different 3d transition metals have been studied.[43,44] For example, ferric wheels Fe_n (for even $n = 6 - 18$) have been reported,[45–50] showing antiferromagnetic (AF) coupling between the $S_i = 5/2$ spins of the Fe^{3+} ions, resulting in a total $S = 0$ ground state. Chromium wheels of different number of Cr^{3+} ions with spin $S_i = 3/2$ have also been intensively investigated. In particular, $\{Cr_8\}$ with AF coupling and total $S = 0$,[51–54] which served as precursor for the synthesis of other homometallic[55,56] and heterometallic closed[57–61] and open rings[62–66] was thoroughly investigated. The heterometallic $\{Cr_7Ni\}$[67,19] wheel containing an AF coupled Ni^{2+} ion, with a total $S = 1/2$ ground state, has been considered as a candidate for the implementation of molecular qubits.[41,39]

A powerful experimental method to study the on-surface magnetic properties of these polymetallic clusters is X-ray absorption spectroscopy (XAS) combined with X-ray magnetic circular dichroism (XMCD). Pertinent to the present work are previous XAS – XMCD studies of Cr^{3+} wheels as monolayer (ML) or polycrystalline thin-films (TFs). In early works on Cr_8-piv ($S = 0$) and Cr_7Ni-piv[68] ($S = 1/2$) TFs deposited by drop casting, XMCD was crucial to determine the AF nature of interactions and the resulting ground state. In a comparative study of the magnetic properties of TF and sub-ML distributions of Cr_7Ni wheels grafted on Au(111), functionalized through S-ligands (Cr_7Ni-3tpc), S-free derivatives (Cr_7Ni-4mtpp) and other approaches (Cr_7Ni-phenoxy, CoPc-Cr_7Ni),[39] XMCD allowed to correlate the Ni dichroic signal with the strength of ligand-substrate bonding. An XMCD study of the magnetic properties of sub-ML distributions of isolated molecular Cr_7Ni rings either deposited or grafted on Au(111) by liquid phase showed a weakening of the Ni–Cr bond, which was associated to slight ring distortions.[69]

M. Panighel
CNR-IOM
Laboratorio TASC
Basovizza, Trieste 34149, Italy
M. Panighel, A. Mugarza
Catalan Institute of Nanoscience and Nanotechnology (ICN2)
CSIC and BIST
Campus UAB
Barcelona 08193, Spain
A. Mugarza
ICREA – Institució Catalana de Recerca i Estudis Avançats
Barcelona 08010, Spain
M. Rancan
Institute of Condensed Matter Chemistry and Technologies for Energy (ICMATE)
National Research Council (CNR)
c/o Department of Chemical Sciences
University of Padova
via F. Marzolo 1, Padova 35131, Italy
L. Armelao
Department of Chemical Sciences and Materials Technologies (DSCTM)
National Research Council (CNR)
Piazzale A. Moro 7, Roma 00185, Italy

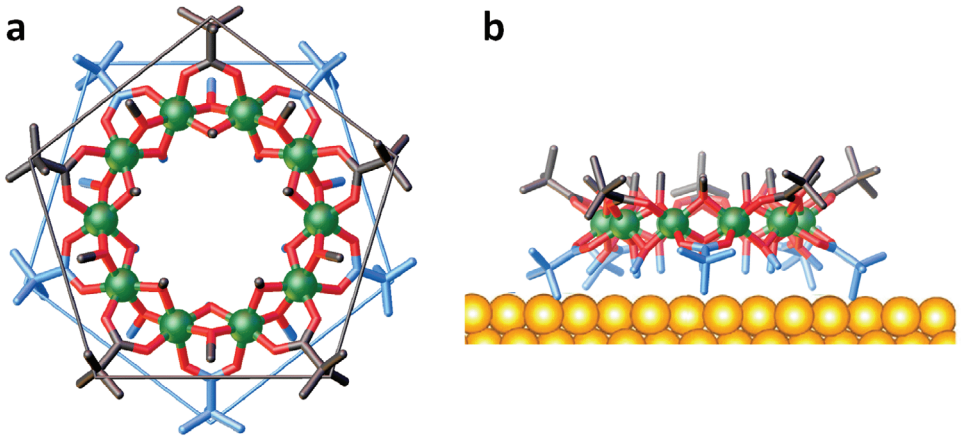

Figure 1. a) Structure of the $\{Cr_{10}(OMe)_{20}(O_2CCMe_3)_{10}\}$ wheel, top view. The close to fivefold symmetry of carboxylate ligands (right) has been outlined by lines connecting the tert-butyl groups above and below the metal ring plane; b) Schematics of $\{Cr_{10}\}$ deposited on Au(111), lateral view. Color code: Cr green, O red, C black (light blue) atoms above (below) the plane of metal atoms ring.

The different magnetic properties and anisotropy of ML and TFs of Cr_7Ni-bu self-assembled by sublimation on Au(111), non-flat wheels deposited on HOPG[70] and Cr_7Ni-thiobu grafted on Au(111) by functionalization were discussed in ref. [19]. Finally, in the study of polycrystalline TFs of $Cr_{2n}Cu_2$ rings,[71] XMCD was used to locally probe the moment of Cr and Cu ions and discuss the question of entanglement.

In view of obtaining SMM behavior, ferromagnetic (FM) coupling between the metallic ions is necessary. However, most homometallic wheels are AF coupled,[72,73] whereas FM coupled instances are much scarcer, for example, $\{Cu^{II}_6\}$, $\{Mn^{II}_6\}$,[43] $\{Ni^{II}_{12}\}$, and $\{Co^{II}_{12}\}$.[44] Interestingly, the study of the family of Cr^{3+} wheels $[Cr_{10}(OR)_{20}(O_2CR')_{10}]$, (with R′ = Me, R = Me (**1**), Et (**2**); R′ = Et, R = Me (**3**), Et (**4**); R′ = CMe_3, R = Me (**5**), Et (**6**)), revealed a remarkable dependence of the magnetic coupling with R and R′ ligands.[74] From $\chi(T)$ susceptibility measurements on powdered samples, it was concluded that **1** and **5** showed an overall FM behavior (with an estimated average interaction constant equal to $J/k_B = +5.3$ K for **1**, and weaker, $J/k_B = +0.59$ K, for **5**), whereas all other compounds showed an overall AF behavior. Inelastic Neutron Scattering (INS) studies of **1** revealed the overall interaction constant had to be an average of five distinct J_{ij} between Cr_i^{3+}-Cr_j^{3+} pairs, and suggested the existence of a zero-field-splitting (ZFS) with a negative anisotropy constant D in the Hamiltonian, $\mathcal{H}_{ZFS} = D(S_z^2 - S(S+1)/3)$. Subsequent electron paramagnetic resonance (EPR) measurements of **5** (hereafter $\{Cr_{10}\}$)[75] showed this wheel behaves as a SMM with a uniaxial anisotropy, $D/k_B = -0.045 \pm 0.004$ K and a cluster $S = 9$ ground state.

Very recently, we unveiled the origin of this intermediate $S = 9$ ground state in $\{Cr_{10}\}$.[76] Its magnetic properties could be rationalized within a model where $\{Cr_{10}\}$ is formed by two semi-wheels, each with four Cr^{3+} spins FM coupled, separated by two Cr^{3+} ions AF coupled asymmetrically (vide infra, **Figure 9a**). INS allowed us to confirm this coupling model leading to the $S = 9$ ground state, and first excited state $S = 8$. SMM behavior with an activation energy of $U/k_B = 4.0(5)$ K was measured, in very good agreement with the expected value $U/k_B = (D/k_B)S_z^2 = 3.6(4)$ K from the EPR experimental value of D. We showed that the unusual behavior of $\{Cr_{10}\}$ arises from the asymmetry in the molecule interactions produced by small distortions in the angles of the Cr–O–Cr alkoxy bridges coupling the Cr^{3+} ions.

Remarkably, some of us succeeded in depositing $\{Cr_{10}\}$ on a Ag(110) single-crystal[20] by UHV sublimation, paving the way for studying the magnetic properties of these interesting wheels self-assembled onto different substrates. In this work, we present the magneto-structural properties of UHV-sublimated $\{Cr_{10}\}$ wheels on Cu(111) and Au(111) metallic substrates, investigated combining scanning tunneling microscopy (STM), X-ray photoelectron spectroscopy (XPS), X-ray absorption spectroscopy (XAS), X-ray natural linear dichroism (XNLD) and X-ray magnetic circular dichroism (XMCD). We discuss the field dependence of the magnetization and the magnetic anisotropy of the deposited $\{Cr_{10}\}$ molecules as a function of the metallic substrate and coverage. We compare the magnetic behavior of the films with that of bulk $\{Cr_{10}\}$.[74,76] Monte Carlo simulations have been used to rationalize the modified magnetic properties of surface-deposited monolayer samples.

2. Preparation of On-Surface $\{Cr_{10}\}$ Samples

2.1. Structure of the Initial $\{Cr_{10}\}$ Single-Crystals

$\{Cr_{10}(OMe)_{20}(O_2CCMe_3)_{10}\}$ (from now on $\{Cr_{10}\}$) single crystals were prepared by a solvothermal reaction using a method previously described.[20] The crystal structure was checked by X-ray diffraction and coincided with that described by D.M. Low et al. (triclinic S.G. $\bar{P}1$).[74] The $\{Cr_{10}\}$ cyclic structure is formed by 10 Cr^{3+} ions lying close to an equatorial plane (**Figure 1**). The ring diameter is about 0.96 nm considering two opposite Cr atoms, while it is close to 1.7 nm when considering the C atom connecting the three methyl groups of the tert-butyl crown. Taking into account all the atoms of the molecule, it occupies a room of diameter ≈ 2 nm. Each pair of Cr–Cr ions is bridged by one μ_2-carboxylate and two μ_2-alkoxide groups. The carboxylate groups are alternatively oriented above and below the $\{Cr_{10}\}$ plane, but all of them point away from the ring. The wheel presents a close to fivefold symmetry. The mean distance between two tert-butyl groups above or below the metal ring is about 1 nm. The alkoxide groups between nearest neighbor (n.n.) Cr^{3+} ions point toward

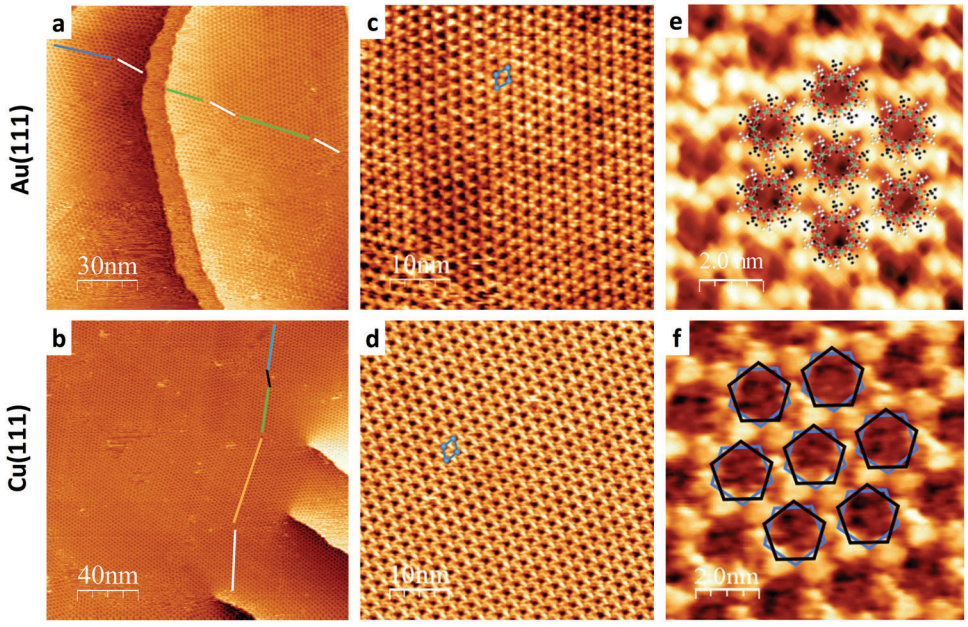

Figure 2. STM images of $\{Cr_{10}\}$ monolayers on Au(111) (top) and Cu(111) (bottom). The existence of mosaicity is outlined in (a,b). The wheels' close to fivefold symmetry close-packed model is superimposed on high resolution STM images (e,f). The quasi-hexagonal unit cells are outlined on the large-scale images (c,d). a) 150 × 150 nm^2, 1200 mV, 0.6 nA; b) 200 × 200 nm^2, 1000mV, 1.2nA; c) 50 × 50 nm^2, 1300 mV, 0.200 nA; d) 50 × 50 nm^2, 875 mV, 1.500 nA; e) 10 × 10 nm^2, 1300 mV, 0.200nA; f) 10 × 10 nm^2, 1200 mV, 0.092 nA.

and away from the wheel, respectively, with one lying above and the other below the metal plane (Figure S1, Supporting Information).

Since there is only one $\{Cr_{10}\}$ molecule per unit cell the crystal can be viewed as packed in columns with all the molecules showing the same orientation. Although the stacking direction is parallel to the crystallographic *a*-axis, the axis perpendicular to the molecule's mean plane (*z*-axis) is ≈35°away from the *a*-axis. Alternatively, the stacking of molecules can be visualized as layers of molecules at slightly different heights with a common *z*-axis perpendicular to the molecular ring's plane, but with slight relative shifts between layers. The average distance between these layers of molecules is ≈0.8 nm (Figure S1, Supporting Information).

2.2. Preparation and Structure of Substrate-Supported $\{Cr_{10}\}$

$\{Cr_{10}\}$ molecules were successfully sublimated onto Au(111) and Cu(111) single-crystal substrates, at conditions similar to those earlier used for the sublimation on Ag(110).[20] $\{Cr_{10}\}$ were deposited from a pyrolytic boron nitride crucible held at temperatures between 520 and 540 K on the Cu or Au substrates, held at room temperature, previously cleaned by repeated cycles of 1 keV Ar^+ sputtering and annealing. On-surface $\{Cr_{10}\}$ samples of different thickness could be grown by tuning the deposition time. Surface coverage was monitored in situ by STM at room temperature. Figure S2, Supporting Information, shows STM images of sub-monolayers of $\{Cr_{10}\}$ on the two studied substrates. After a deposition time of 10′, 1ML coverage of $\{Cr_{10}\}$ on Au(111) and Cu(111) over large areas were obtained, as shown in the large-scale STM images reported in **Figure 2a**,**b**. The STM images of the $\{Cr_{10}\}$/Au(111) and $\{Cr_{10}\}$/Cu(111) monolayers in Figure 2c,d reveal that the wheels self-assemble in an ordered hexagonal structure, as shown by the unit cells outlined in the images in blue. The analysis of many STM images yields a hexagonal unit cell of dimension 2.3 ± 0.1 nm, similar in both substrates, within the experimental error.

The higher resolution images (Figure 2e,f) show that the wheels retain their structure and exhibit a close to fivefold symmetry: at each $\{Cr_{10}\}$ molecule position, the black pentagons evidence the bright spots attributed to the tert-butyl groups of the carboxylate ligands above the equatorial metal plane and the second blue pentagon, rotated by 36° with respect to the former, can be ascribed to the tert-butyl groups below the metal plane. The average pentagon side length is close to 1 nm, which agrees with the distance of tert-butyl groups below or above the equatorial plane of the molecule (Figure S1, Supporting Information). The close-packed, quasi-hexagonal 2D network, shown by the high resolution STM contrast is very similar to that earlier described for monolayer $\{Cr_{10}\}$/Ag(110).[20]

The large scale STM images reported in Figure 2a,b evidences the presence of many hexagonal domains slightly rotated relative to each other. This suggests that the molecules are relatively free to move on the surface and aggregate with each other in the 2D assembly. The long-range order of the sublimated monolayers in correlation with that of the surface was further investigated by Low-Energy Electron Diffraction (LEED). In line with the STM observations, the LEED experiments do not show a clear diffraction pattern typical of commensurate overlayers, but rather diffuse halos. Nonetheless, the comparison of the LEED images for 1ML $\{Cr_{10}\}$ on Cu and on Au shows interesting differences: the pattern obtained on Cu(111) at 28 eV (Figure S3a, Supporting Information) shows an hexagonal pattern of rather

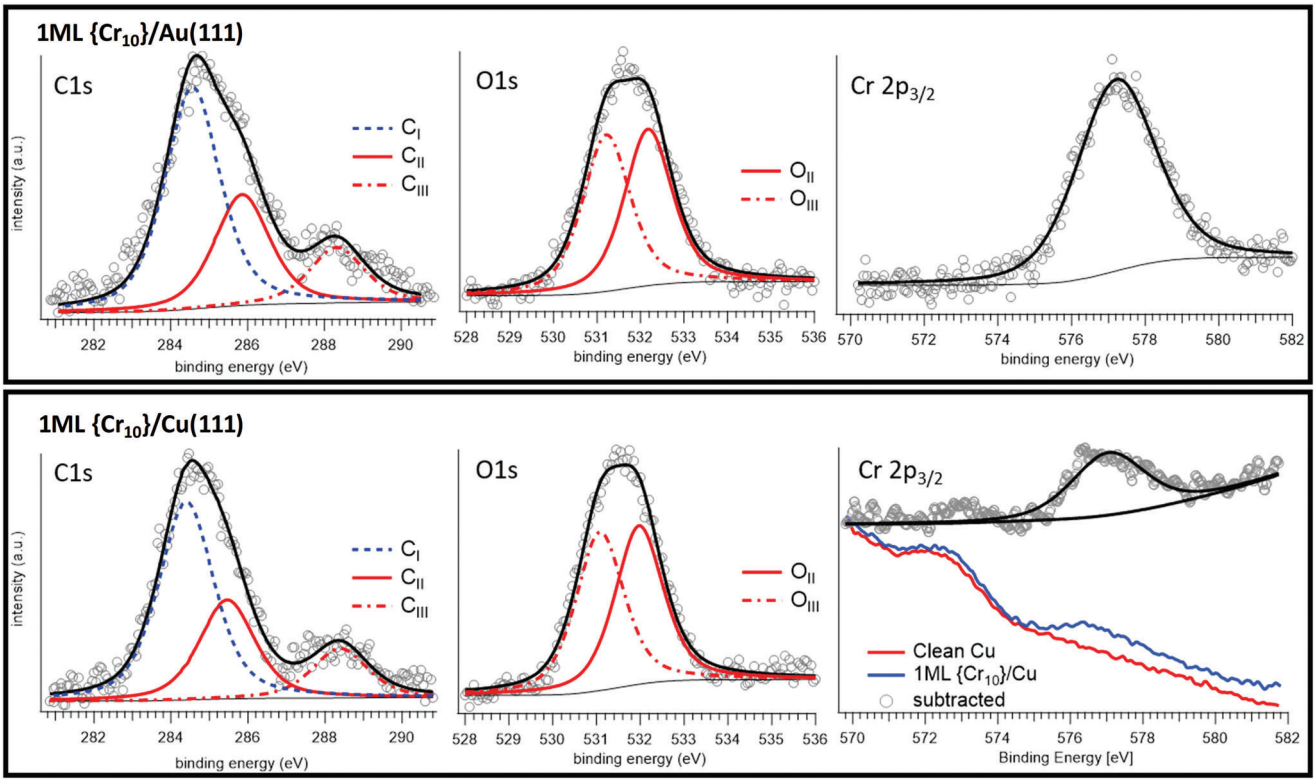

Figure 3. XPS measurements of the 1ML $\{Cr_{10}\}$/Au(111) sample (top) and 1ML $\{Cr_{10}\}$/Cu(111) sample (bottom) at the C1s region (left), O1s region (center) and Cr2$p_{3/2}$ region (right).

large spots in the same direction of the substrate spots (85 eV), whereas the pattern obtained on Au(111) does not shows any overlayer spots at 30 eV (Figure S3b, Supporting Information), and also the substrate spots appears quite faint (76 eV). Therefore, the LEED data suggest a higher level of epitaxial order on Cu(111) than on Au(111), which probably implies a stronger vertical interaction between the molecules and the Cu(111) substrate.

X-ray Photoelectron Spectroscopy (XPS) measurements further confirm the integrity of sublimated $\{Cr_{10}\}$ wheels on Au(111) and Cu(111). The complete XPS analysis of the C 1s, O 1s, and Cr $2p_{3/2}$ peaks performed on 1ML samples deposited on both surfaces is reported in **Figure 3** and Supplementary (Figures S4 and S5, Supporting Information). In the C 1s region, the XPS signal is deconvoluted in three peaks in accordance with the molecular structure: C_I ascribed to aliphatic carbon in the tert-butyl groups ($-C_4H_9$), C_{II} associated to oxygen-bound carbon of methoxy groups ($-OCH_3$), and C_{III} the electron-depleted carbon of carboxylate groups (COO). The area ratio of the three components is $4C_I$:$2C_{II}$:$1C_{III}$ in agreement with the expected nominal values for intact $\{Cr_{10}\}$ wheels.

O 1s peaks have been fitted with two components with the same area in agreement with the stoichiometry of the two types of oxygen present in the molecules respectively in the carboxylate (O_{III}) and in the methoxy (O_{II}) groups, $1O_{III}$:$1O_{II}$. The O_{III} bending energy (BE = 531.2 eV) has been assigned to the carboxylate groups by comparison with the O 1s high resolution spectrum of $\{[Cr_6F_7(O_2CCMe_3)_{10}][NH_2Et_3]_3\}_2$[77] (O 1s, BE = 531.5 eV in Figure S6c, Supporting Information), precursor of the $\{Cr_{10}\}$ wheel. This compound contains Cr^{3+} ions with a similar carboxylic environment, but without methoxy ligands.

The binding energy position of the Cr $2p_{3/2}$ peak is in perfect agreement with the expected Cr^{3+} oxidation state. It is important to note that in the case of $\{Cr_{10}\}$ on Cu(111) the Cr $2p_{3/2}$ peak is partially superimposed to the Cu_{LMM} Auger signal, thus, to evidence the position of the peak in Figure 3 we report the signal obtained after subtracting the peak of clean Cu to the peak of 1ML$\{Cr_{10}\}$/Cu(111).

The shape and the binding energy position of these peaks are very similar regardless of the metal substrate, and quantitative analysis of C 1s, O 1s, and Cr $2p_{3/2}$ peaks, reported in Figures S4 and S5, Supporting Information, yield C/O, C/Cr, and O/Cr atomic ratios in agreement with intact $\{Cr_{10}\}$. Moreover, the XPS peaks observed in monolayer samples were coincident with those found in bulk $\{Cr_{10}\}$, as shown in Figures S6 and S7, Supporting Information, further confirming the integrity of the molecules.

Additionally, to verify the integrity of $\{Cr_{10}\}$ in multilayer samples, XPS analysis was conducted on samples with increasing thicknesses. In Figure S8, Supporting Information, we report for comparison the XPS C 1s, O 1s, and Cr $2p_{3/2}$ peaks of the monolayer and two different multilayer coverages on Cu(111). The increase of the peaks area is linear with the deposition time. Moreover, the shape of the peaks and the area ratio is constant at different coverages, indicating that the molecules keep their structure also for thicker films.

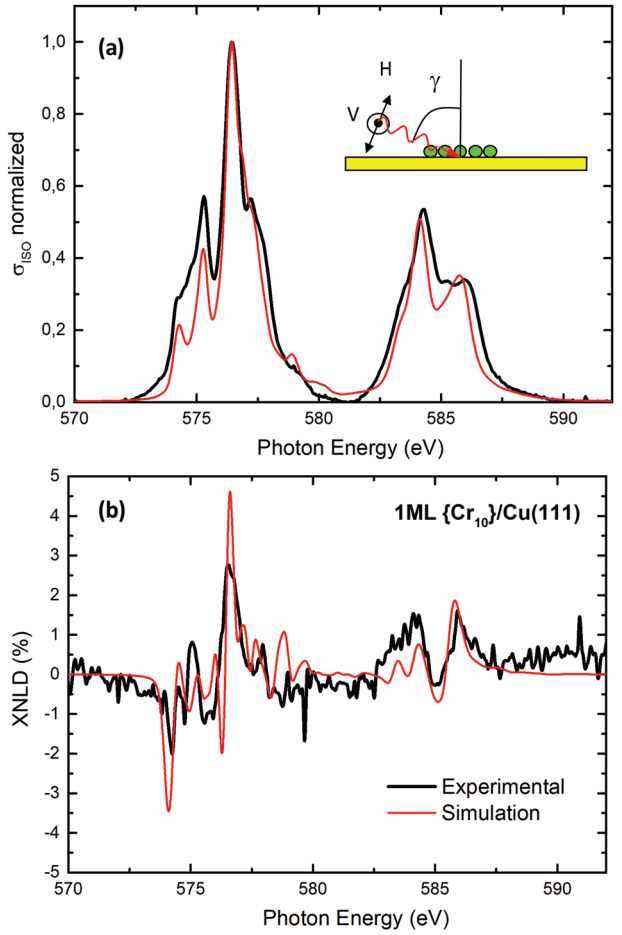

Figure 4. a) Experimental (black) and calculated (red) isotropic XAS, defined as $\sigma_{ISO} = (\sigma_{\parallel} + 2\sigma_{\perp})/3$, with $\sigma_V = \sigma_{\perp}$, and $\sigma_H = (\sin^2\gamma)\sigma_{\parallel} + (\cos^2\gamma)\sigma_{\perp}$ for $\gamma = 70°$ (see Supporting Information S4 and ref. [23] for details). Inset: sketch of the experimental configuration for XNLD experiments: H is parallel to the synchrotron ring plane, and V perpendicular to it; b) experimental (black) and calculated (red) XNLD spectra ($\sigma_V - \sigma_H$), normalized to the isotropic signal, for sample 1ML $\{Cr_{10}\}$/Cu(111).

In the bulk the $\{Cr_{10}\}$ wheels are packed along the *a*-axis, with the distance between adjacent molecules being 0.987 nm. If the deposited molecules would follow the same structure, the wheels would not be placed just on top of those of the first layer, but slightly shifted, with the distance between layers being ≈0.8 nm (see Figure S1b, Supporting Information). Unfortunately, high-resolution STM images of 2ML samples could not be obtained, as the tip scanning produced the movement of the top-most layer; hence, the actual packing of $\{Cr_{10}\}$ in multilayer samples could not be ascertained.

In the remaining of this work, we will discuss magnetic results obtained on monolayer (1ML) samples of $\{Cr_{10}\}$ on Cu(111) and Au(111), to investigate the influence of the substrate, and a sample with an estimated number of 14 monolayers (14ML) to study the influence of the layer addition on the magnetic properties of deposited $\{Cr_{10}\}$.

3. Magnetic Properties of Deposited $\{Cr_{10}\}$

The magnetic properties of monolayer samples on two different substrates, 1ML $\{Cr_{10}\}$/Cu(111), 1ML $\{Cr_{10}\}$/Au(111), and a thin 14ML $\{Cr_{10}\}$/Au(111) sample, were studied under synchrotron radiation at low temperature ($T = 3.4$ K). In situ STM experiments were performed to guarantee the formation of extensive monolayers.

First, to assess the electronic anisotropy of Cr^{3+} ions in the deposited $\{Cr_{10}\}$ molecules we investigated the X-ray Natural Linear Dichroism (XNLD) by measuring the X-ray Absorption Spectra (XAS) using vertically (V) and horizontally polarized light (H), with respect to the synchrotron ring plane, at the Cr $L_{2,3}$ edge, under grazing incidence ($\gamma = 70°$) and zero applied field. The electric field vector $\boldsymbol{E}$ of linearly polarized X-ray acts as a "searchlight" for the valence band empty states in different directions of the atomic volume. For the selected experimental geometry, $\boldsymbol{E}_V$ lies in the sample substrate plane for V, while $\boldsymbol{E}_H$ is mostly out-of-plane (see sketch in the inset of **Figure 4**). The XNLD signal is defined as the difference, $\sigma_V - \sigma_H$, between the cross-sections measured with vertically polarized (σ_V) photons and with horizontally polarized (σ_H) photons. Figure 4a shows the XNLD signal measured for the 1ML $\{Cr_{10}\}$/Cu sample, normalized to the isotropic adsorption spectrum σ_{ISO}, calculated from the measured σ_V and σ_H values at $\gamma = 70°$. (A similar XNLD signal was measured for the 1ML $\{Cr_{10}\}$/Au sample, see Figure S10, Supporting Information). A small XNLD signal of 3.6% is detected, which is of pure electronic origin, as measurements were performed under $H = 0$.

We simulated the observed XNLD signal within the framework of the ligand field multiplet approach implemented in Quanty-Crispy code (see Supporting Information **S5** for details). The $\{Cr_{10}\}$ molecule can be viewed as a ring of $[CrO_6]$ octahedra connected by two sharing O^{2-} ions. Each of the octahedra is oriented such that one of its trigonal axes is nearly parallel to the normal **n** to the molecule's mean plane and substrate (Figure S9, Supporting Information). Thus we simulated the XNLD of a single Cr^{3+} under trigonal symmetry (C_{3v}) for incident X–ray **k**(1,0,0) and polarizations $\boldsymbol{E}_H$ (0,0,1) and $\boldsymbol{E}_V$ (0,1,0). As shown in Figure 4, the experimental XNLD and isotropic XAS could be nicely reproduced considering a cubic crystal field splitting of $Dq = 0.195$ eV and small distortions from the octahedral symmetry, $D\sigma = 0.045$ eV, $D\tau = 0.01$ eV. This value of Dq is quite comparable to the value 0.2182 eV given by Mc Clure[78] for Cr^{3+}. The same simulation parameters could be used to satisfactorily reproduce the XAS and XMCD spectra at 6 T (vide infra). The slight overestimation of the calculated XNLD signal may be attributed to the existence of an angular distribution of the ten different single-ion Cr^{3+} trigonal axes from the normal to the molecular plane, and disorder induced by the mosaicity within the deposited 1ML.

To characterize the magnetic properties of sublimated $\{Cr_{10}\}$, XAS measurements under left (C^-) and right (C^+) circularly polarized light and X-ray magnetic circular dichroism (XMCD) at the Cr $L_{2,3}$ edge were performed under a magnetic field of $\mu_0 H = 6$ T at $T = 3.4$ K, for different beam incidence angles with respect to the substrate normal (γ). **Figure 5a–c** shows the XAS and XMCD spectra measured for the 1ML $\{Cr_{10}\}$/Cu, 1ML $\{Cr_{10}\}$/Au, and 14ML $\{Cr_{10}\}$/Au samples in normal incidence ($\gamma = 0°$). Qualitatively, the spectra for all the samples are very similar. The XAS

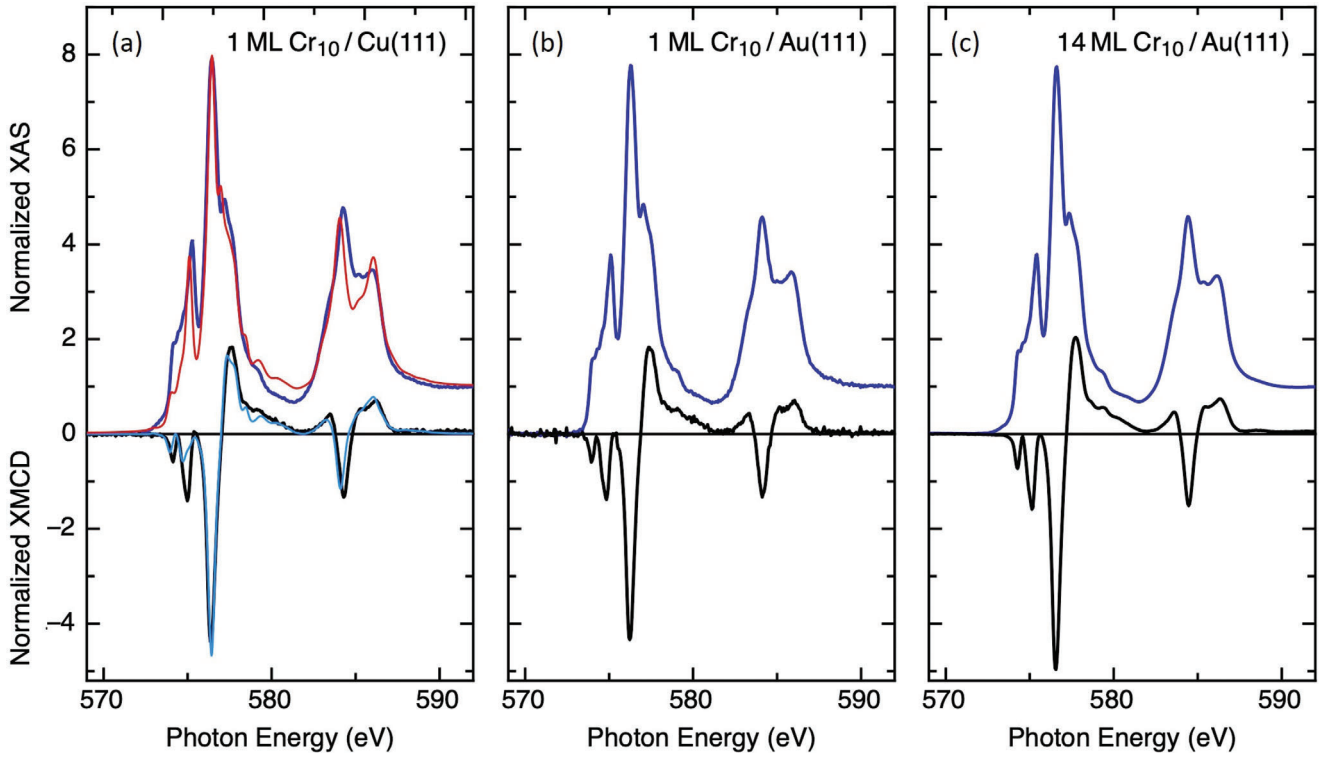

Figure 5. Cr $L_{2,3}$ XAS (top) and XMCD (bottom) normalized spectra measured at $T = 3.4$ K, $\mu_0 H = 6$ T in normal beam incidence ($\gamma = 0°$) for a) 1ML {Cr_{10}}/Cu(111), b) 1ML {Cr_{10}}/Au(111), and c) 14ML {Cr_{10}}/Au(111). In (a), the simulated XAS and XMCD spectra are also shown, see Supporting Information S5 for details. A double-step function was added to the simulated whiteline to enable the comparison with the experimental XAS.

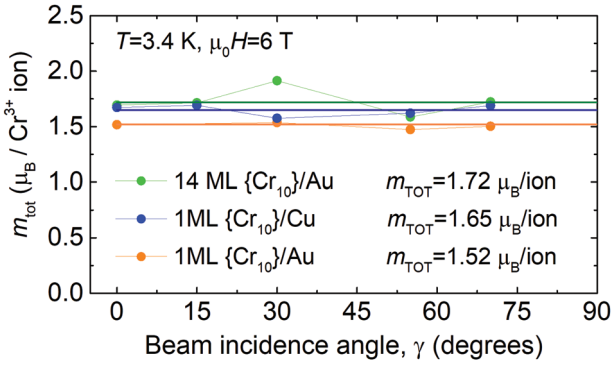

Figure 6. Angular dependence of the total magnetic moment, $m_{tot}(\gamma)$ at $T = 3.4$ K, $\mu_0 H = 6$ T, for the three studied {Cr_{10}} deposited samples. The spin correction factor $SC = 1.75$ in Equation (2) was applied.

line at the L_3 edge displays a shoulder (574.11 eV), 3 peaks at 575.26, 576.45, 577.24, and a satellite at 579.21 eV, while L_2 shows a main peak at 584.24 eV and a smaller one at 586.04 eV. These features are typical of Cr^{3+} in an octahedral environment, as previously observed.[68] The XMCD signal exhibits two distinct peaks below the large negative L_3 peak. The XAS – XMCD spectra could be nicely reproduced by multiplet simulations (see Figure 5a), using the same parameters used to simulate the XNLD. This result agrees with the minor distortions of the octahedral coordination geometry of Cr^{3+} ions, which shows a continuous shape measure (CShM) value of 0.885, calculated with SHAPE2.1[79] from the crystallographic data of the bulk {Cr_{10}} sample.[74]

To search for magnetic anisotropy of {Cr_{10}} supported on surface, we measured the XAS and XMCD spectra as a function of γ. A small angle dependence in the XMCD spectrum is observed when passing from $\gamma = 0°$ to $\gamma = 70°$, accompanied by a change in the XAS amplitude, so that the magnetic anisotropy of the normalized XMCD spectra is practically unobservable. A similar result was previously reported for {Cr_7Ni} wheels.[70]

Quantitative magnetic moments were obtained by applying the sum rules to the angle-dependent XAS and XMCD spectra. For the number of holes in the 3d band we considered the nominal value $N_{eff} = 7$ for Cr^{3+}. The dipolar term $\langle T_z \rangle$ is expected to be negligible for Cr^{3+} ions in O_h symmetry;[80] however, to avoid this pre-assumption, we calculated the effective spin moment $m_s^{eff}(\gamma) = m_S - 7m_T(\gamma)$, and deduced only a posteriori the maximum contribution of the $7m_T$ dipolar term. Thus, we determined the orbital magnetic moment (m_L) and effective magnetic moment (m_s^{eff}) per Cr^{3+} ion as:

$$\frac{m_L}{\mu_B} = -\frac{4qN_{eff}}{3r} \quad (1)$$

$$\frac{m_s^{eff}}{\mu_B} = -\frac{(6p-4q)\,N_{eff}}{r} SC \quad (2)$$

where r is the integral of the background-subtracted absorption spectrum, A and B are the intensities of the dichroic signal at L_3 and L_2 edges, respectively, and $p = A$ and $q = A + B$. The

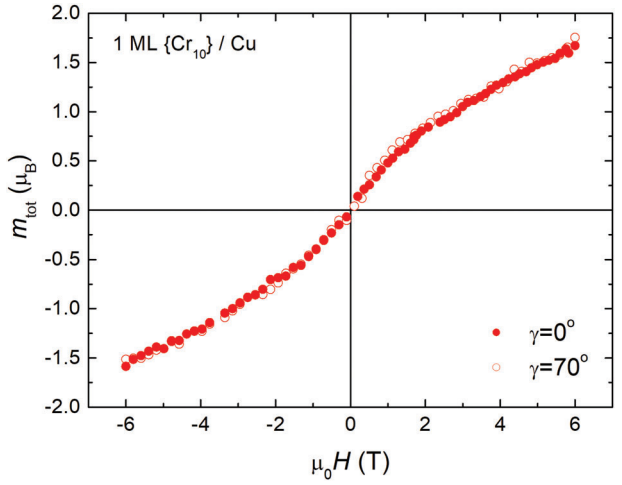

Figure 7. Field dependence of the total magnetic moment per Cr^{3+} ion at $\gamma = 0°$ and $\gamma = 70°$ beam incident angles, $T = 3.4$ K, for sample 1ML $\{Cr_{10}\}$/Cu.

spin correction *SC* is required to account for the partial L_2 and L_3 mixing in Cr.[81] We used a value $SC = 1.75$, which had been previously validated for Cr_8 and Cr_7Ni-piv[68] and applied to other Cr rings,[69,70,82] given that the Cr $L_{2,3}$ absorption spectrum of $\{Cr_{10}\}$ is identical to that of the aforementioned compounds. The value of the intrinsically isotropic spin moment was determined as the value of the effective moment at the so-called "magic angle," at which the dipolar term cancels in paramagnetic systems, that is, $m_s = m_s^{eff}$ ($\gamma = 54.7°$).[83,84] Then, the angular dependence of the total magnetic moment was calculated as: $m_{tot}(\gamma) = m_s + m_L(\gamma)$.

From this quantitative analysis the following conclusions can be drawn. First, the orbital magnetic moment is negligible, within the experimental error, which agrees with $m_L \approx 0$ for Cr^{3+} in $\{Cr_8\}$ and $\{Cr_7Ni\}$ wheels reported by Corradini et al.[68] Second, the dipolar contribution $7m_T$ is estimated to be at most ≈10% of m_s^{eff}, so m_T is within the experimental uncertainty. And finally, there is no detectable local anisotropy at this temperature, as can be observed in **Figure 6**, from the hardly noticeable angle dependence of $m_{tot}(\gamma)$. The total magnetic moment values determined for the three studied samples at 3.4 K and 6 T are summarized in Figure 6.

The magnetic field dependence of the dichroic signal XMCD(*H*), was measured at $T = 3.4$ K changing the helicity of the beam at fixed incident photon energy corresponding to the maximum XMCD signal (576 eV) and ramping the magnetic field from 6 to −6 T, and from −6 to 6 T. Measurements were carried out in normal ($\gamma = 0°$) and grazing ($\gamma = 70°$) incidence. The absolute *y*-axis value was determined by scaling the XMCD(*H*) cycles to the total magnetic moment obtained from the sum rules at 6 T. **Figure 7** shows the XMCD(*H*) curve for the 1ML $\{Cr_{10}\}$/Cu sample, while the data for the 1ML $\{Cr_{10}\}$/Au and 14ML $\{Cr_{10}\}$/Au samples are collected in Figure S12, Supporting Information. The magnetization exhibited no hysteresis in any of the three studied samples. Moreover, no difference was observable between the $m_{tot}(H)$ curves at $\gamma = 0°$ and $\gamma = 70°$ at any magnetic field value, within experimental resolution. These results indicate that the $\{Cr_{10}\}$ cluster anisotropy is too small to

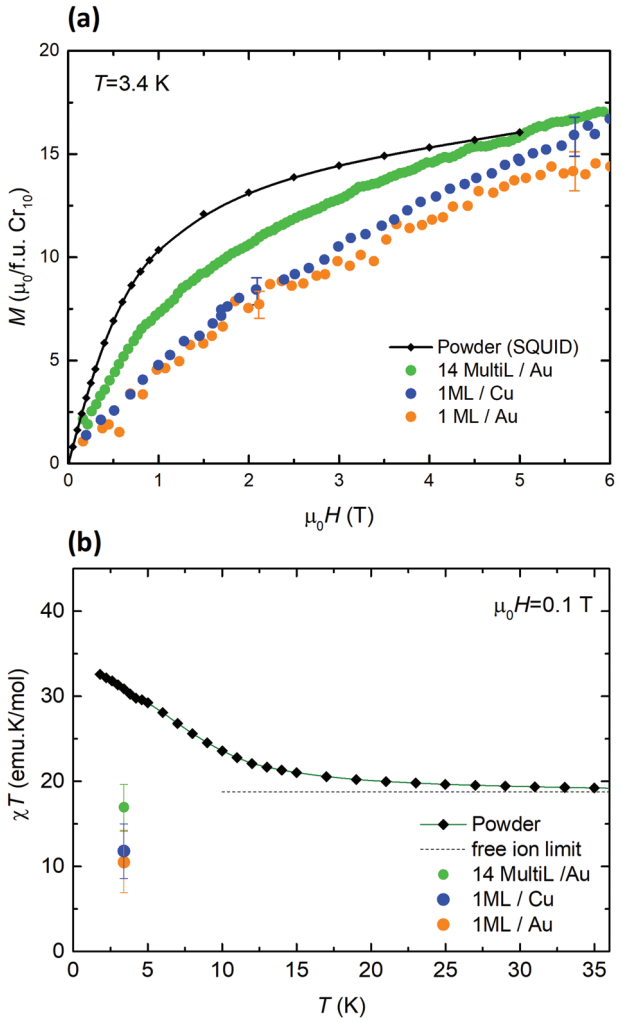

Figure 8. a) Comparison of the magnetization of the $\{Cr_{10}\}$ wheel as a function of the applied field, $M(H) = 10m_{tot}(H)$, for samples 1ML/Cu, 1ML/Au, and 14ML/Au obtained by XMCD at $T = 3.4$ K, $\mu_0 H = 6$ T. For comparison, the magnetization measured for the bulk at the same temperature (3.4 K) is shown; b) Comparison of the susceptibility-temperature product, $\chi T(T)$ at 0.1 T, for the bulk and $\{Cr_{10}\}$ layered samples at 3.4 K.

enable the observation of SMM behavior at the temperature of experiment (3.4 K). We note that the SMM behavior in (Fe_4), with an energy barrier of $U/k_B \approx 16$ K larger than that measured for $\{Cr_{10}\}$ in bulk ($U/k_B \approx 4$ K)[76] or that predicted for monolayers (U/k_B≈1.3-3.1 K, vide infra), could only be observed at sub-kelvin temperatures.[34]

Figure 8a compares the field-dependence of the total magnetic moment per Cr^{3+} ion measured in normal incidence ($\gamma = 0°$) for the three on-surface studied samples, together with the curve measured for powder $\{Cr_{10}\}$ at the same temperature (3.4 K) for the sake of comparison. The monolayers show magnetizations clearly lower than that of the $\{Cr_{10}\}$ molecules in the bulk material, except at the highest applied magnetic field values, while the 14ML $\{Cr_{10}\}$/Au sample displays an intermediate magnetic behavior. (It is noted that the experimental curve reflects the magnetic behavior of the outermost 5–6 layers of the 14ML sample, as XMCD in TEY probes only a few nanometers into the

sample). Figure 8b compares the susceptibility-temperature product, χT, for the layered samples at 0.1 T and 3.4 K (obtained from the initial slope of the $M(H)$ curves) with the $\chi T(T)$ curve reported earlier for bulk $\{Cr_{10}\}$. It is clear that deposition onto the surface brings along a reduction of the overall FM behavior.

The significant observed changes in the $M(H)$ and $\chi T(T)$ curves must be related to the accommodation of the $\{Cr_{10}\}$ molecules onto the substrate and the subsequent modification of Cr–O–Cr angles on which exchange coupling constants are very dependent.[76,85] Moreover, this change seems to be progressive as additional layers are deposited, with an apparent tendency toward the magnetic behavior of the molecules in the bulk crystalline form. As it will be shown below, the low values of the magnetization at low and intermediate magnetic fields with respect to the single crystal results can be explained consistently as a slight change in the exchange interactions giving rise to a lower spin ground state.

On the other hand, only a small difference between the $m_{tot}(H)$ curves measured for the 1ML $\{Cr_{10}\}$/Au(111) and 1ML $\{Cr_{10}\}$/Cu(111) is observed. Their XAS lineshapes of the MLs on Au(111) and Cu(111) are similar, indicating that the nature of the substrate does not affect the electronic structure of the Cr^{3+} ions. Indeed, due to the local nature of the molecule-substrate bonding, which does not involve any charge transfer, a direct influence of the ligand-substrate bond on the properties of the metal core is not expected. However, since the magnetic properties of the $\{Cr_{10}\}$ wheels seem to depend on their capacity to accommodate to the substrate, differences in the atomic termination of the surface can produce structural changes along the chromium wheel, which can result in slightly different magnetization curves. The distance between n.n. atoms in the two investigated metallic substrates is 0.288 nm for Au(111)[86] and 0.255 nm for Cu(111),[87] hence a difference of ≈15% in the substrate lattice may be enough to produce distortions in the $\{Cr_{10}\}$ wheel affecting the total magnetic moment.

4. Discussion

4.1. Monte Carlo Simulation of Molecular Spin Configurations

In the following we will try to rationalize the observed changes on the magnetic properties of the $\{Cr_{10}\}$ wheels upon deposition onto metallic surfaces. The accommodation of the molecules onto the surface is expected to affect more profoundly the more flexible molecular parts, that is, the outer tert-butyl ligands, than the wheel's skeleton of $[CrO_6^-]$ octahedra connected by edges. However, slight changes in the Cr–O–Cr angles and distances may provoke important modifications in the exchange coupling constants.[76,85] In contrast, the single-ion anisotropies at the Cr^{3+} ions are expected to be much less affected, as they are mainly determined by the full octahedral cage.

Having in mind this central idea, we will explore the consequences of changes in the exchange coupling constants in order to simulate the $M(H)$ curves measured for the ML samples within the framework of the cluster multispin Hamiltonian in terms of the single-ion spins S_i:

$$\mathcal{H}_{CL} = -2\sum_{\langle ij\rangle} J_{ij}\vec{S}_i\cdot\vec{S}_j + \sum_{i=1}^{10} D_i S_{i,z}^2 + g\mu_B\sum_{i=1}^{10}\vec{S}_i\cdot\vec{H} \qquad (3)$$

where the first term describes the exchange interaction coupling, with $\langle i,j\rangle$ denoting the interactions between the nearest neighbor $S_i = 3/2$ spins in the $\{Cr_{10}\}$ ring; spins are numbered from 1 to 10 following the numbering code in **Figure 9a**, previously used in Ref. [76] The second term accounts for the zero-field splitting produced by the single-ion anisotropy of each Cr^{3+} site (D_i), assuming negligible rhombic term, and the last term is the Zeeman splitting with $g \approx 2$.

The single-ion anisotropy parameter was kept unmodified with respect to the $D_i/k_B = -0.31$ K value previously deduced from experimental results for bulk $\{Cr_{10}\}$,[76] under the reasonable assumption that the local environment of each Cr^{3+} ion is not expected to suffer large variations upon on-surface deposition. The total cluster anisotropy D_a and rhombic term E_a in each spin configuration were calculated following the method described by D. Bencini and A. Gatteschi,[88] (see details in section **S8**, Supporting Information).

In order to deal with such a complex system of 10 $S_i = 3/2$ spins in a ring, we used the classical Monte Carlo (MC) method implemented in ALPS[89,90] to calculate $M(H)$ curves, exploring changes in exchange interaction constants J_{ij} starting from the previously proposed distribution of these constants for the bulk system.[76] Different distributions of values of nearest neighbor J_{ij} along the wheel lead to different ground state spin configurations. However, only spin configurations with total spin $S = 0$, 3, 6, 9, 12, and 15 are possible if the local magnetic moments are assumed to be all (almost) parallel or antiparallel. The configurations with $S = 15$ and $S = 12$ can be excluded as their expected magnetization values are too high with respect to those of the present monolayer even at low fields. The spin configuration with $S = 0$ must be also discarded, despite many 3d-wheels reported so far display this AF ground state, because it yields to a close to linear field dependence of the magnetization, incompatible with the experimental results (see Figure S13, Supporting Information).

In the case of bulk $\{Cr_{10}\}$,[76] we could simulate satisfactorily the magnetization $M(H)$ and susceptibility $\chi T(T)$ curves of single-crystalline and powder samples within a $S = 9$ ground state spin configuration model (8 spins up ↑, 2 spins down ↓), with an axial cluster anisotropy of $D_a/k_B = -0.033$ K ($E_a/D_a = 0.15$), assuming no inter-molecular interactions. The n.n. interactions were taken as identical and FM ($J_{FM}/k_B = 2.0$ K), except around two Cr^{3+} ions on opposite sides of the wheel, denoted Cr3 and Cr8 (see Figure 9a for numbering), which were considered AF and asymmetric ($J_{23}/k_B = J_{78}/k_B = -2.0$ K $\neq J_{34}/k_B = J_{89}/k_B = -0.25$ K, $D_i/k_B = -0.31$ K).[76] The same model and exchange interaction constants used for the bulk were tested against the experimental data for the 1ML/Au at 3.4 K (see Figure 9b). The failure of such a model is obvious. Variation of the set of the exchange interaction constants in the $S = 9$ model was unable to bring the simulations near to the experimental curve, that is, in every case the simulated $M(H)$ was too high.

In contrast, a spin configuration with $S = 3$ yields magnetic curves that reproduce reasonably well the experimental results. Indeed, for the case of $S = 3$, two different spin configurations can be considered, denoted S_{3A} and S_{3B}, both respecting the inversion symmetry of the molecule. The experimental data could be well explained within a S_{3A} configuration (Figure 9a,b), with the set of exchange coupling constants

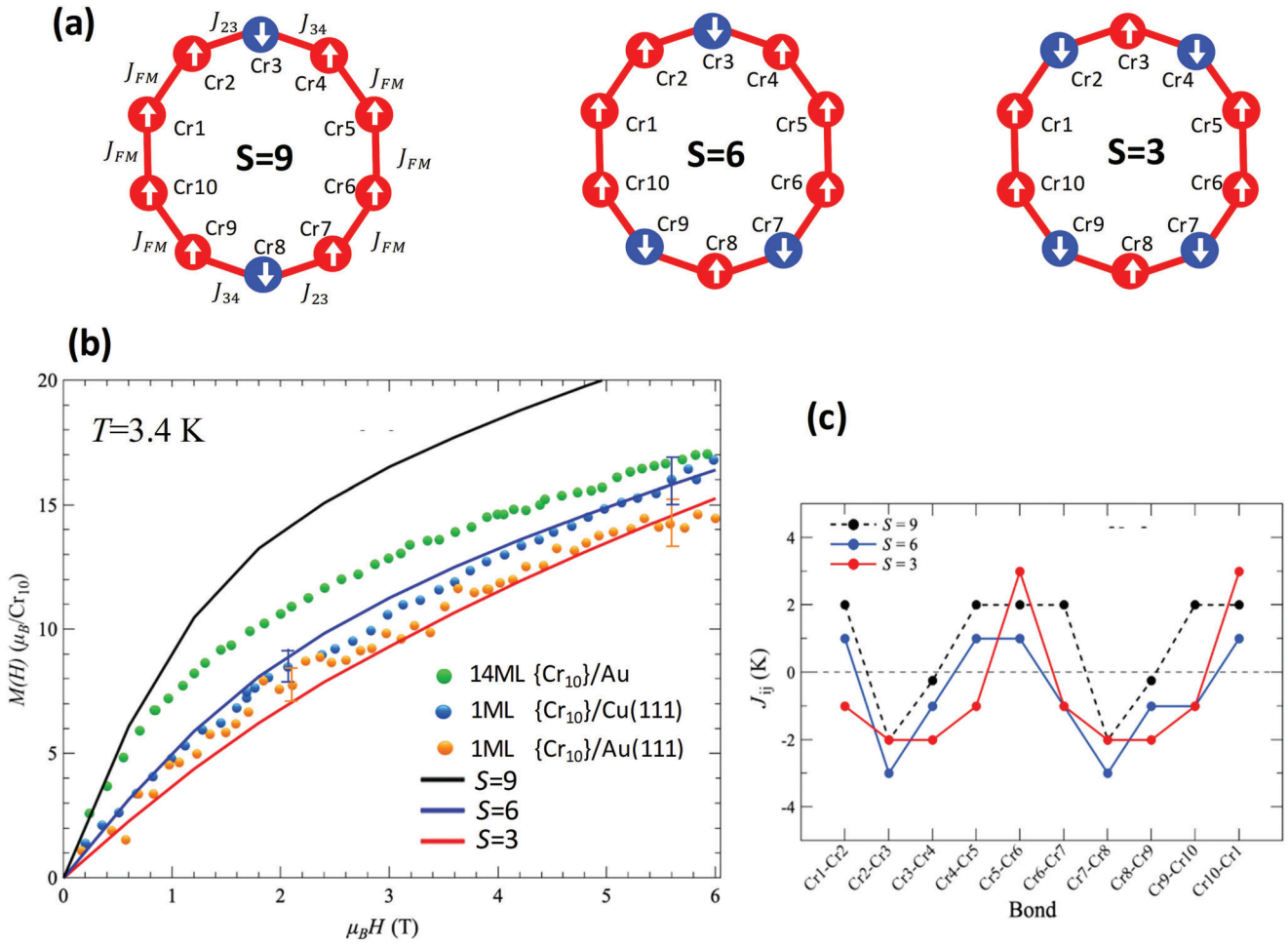

Figure 9. a) Sketch of the ground state of the single spins configurations for total spin $S = 9$, 6, and 3 (S_{3A}). The numbering of the Cr^{3+} spins of the $S = 9$ configuration is that of Ref. [76] and it is also used for the $S = 6$ and $S = 3$ cases; b) Magnetization $M(H)$ curves for the 1ML/Au, 1ML/Cu, and 14ML samples and MC simulations for different spin configurations yielding to a total spin ground state $S = 9$, 6, and 3; c) Plot of the sets of exchange coupling constants J_{ij} for the three cases displayed in (b) following numbering shown in (a).

$J_{12}/k_B = J_{45}/k_B = J_{67}/k_B = J_{9,10}/k_B = -1$ K, $J_{23}/k_B = J_{34}/k_B = J_{78}/k_B = J_{89}/k_B = J_{9,10}/k_B = -2$ K, $J_{56}/k_B = J_{10,1}/k_B = +3$ yielding a mean field value $\langle J\rangle/k_B = -0.6$ K (see Supporting Information **S7**). On the contrary, using the S_{3B} configuration the experimental results cannot be explained by simulations under any set of J_{ij} constants (a sample of results is shown in Figure S14, Supporting Information).

The proposed distribution of J_{ij} values along the wheel for S_{3A} includes only small departures from the values determined for the bulk system. We may note that the mean field value $\langle J\rangle$ is negative, in contrast to the case of the bulk sample, where it was positive, $\langle J\rangle/k_B = +0.59$ K, according to susceptibility measurements. Even though for the monolayer samples the full susceptibility curve $\chi T(T)$ could not be measured directly, the χT determined at 3.4 K is deduced from the slope of the $M(H)$ curve at that temperature, and it is smaller than the expected high T bulk value at 300 K (Figure 8b), supporting the existence of an overall AF mean field value $\langle J\rangle$, as predicted by the MC simulations.

For {Cr_{10}} in the bulk samples, we had previously shown[76] a correlation between the exchange coupling constants J_{ij} and the inner (θ_{inn}) and outer (θ_{out}) Cr–O–Cr angles connecting i and j neighboring Cr^{3+} ions. In particular, the AF exchange coupling constants around the ion labeled Cr3 corresponded to positive $\theta_{inn} - \theta_{out}$ values, while the remaining FM interactions were associated to negative $\theta_{inn} - \theta_{out}$. Therefore, in the case of the {Cr_{10}} monolayers, the sign flip with respect to the bulk case in the J_{ij} interactions for the Cri-Crj couples neighbors to those of Cr3-Cr2 and Cr3-Cr4 could be understood as modifications of the corresponding Cr–O–Cr angles with a sign flip in the difference $\theta_{inn} - \theta_{out}$. Finally, we may note from Figure 9c that the proposed set of J_{ij} values displays a larger symmetry than that of the molecule in the bulk compound ($P\bar{1}$), with an additional mirror plane, which is introduced by the (111) surface of the metallic substrates.

The molecular anisotropy calculated for the S_{3A} configuration, using single ion values $D_i/k_B = -0.31$ K and $E_i = 0$ as in the MC simulations, is $D_a/k_B = -0.14$ K, $E_a/D_a = 0$. Alternatively, recalling that we are assuming that the n.n. environment of the

Cr^{3+} ions may be considered as unchanged upon deposition on the metallic substrates, we can make use of the ab initio results of the bulk compound[76] to compute the molecular anisotropy for the S_{3A} configuration, which produces the compatible values of $D_a/k_B = -0.131$ K and $E_a/D_a = 0.14$. The predicted molecular anisotropy is larger in the 1ML than the bulk $\{Cr_{10}\}$, ($D_a/k_B = -0.033$, $E_a/D_a = 0.15$), as a consequence of the change in the spin configuration produced by the modification of the exchange coupling constants along the wheel.

We have also tested the configuration with ground state $S = 6$, the closest to that found for the bulk compound ($S = 9$). We also found a set of J_{ij} values, with mean field value $\langle J\rangle/k_B = -0.6$ K as in the $S = 3$ configuration, for which the MC simulated $M(H)$ curve approaches the experimental data (Figure 9a,b). This magnetic ground state would not be compatible with the point symmetry group $P\bar{1}$ of $\{Cr_{10}\}$ in bulk, although the point symmetry of the molecule may decrease upon deposition, losing the inversion symmetry. Since we do not have direct experimental evidence for the actual symmetry group of $\{Cr_{10}\}$ on surface, being prudent we can say that although the $S = 3$ spin configuration is more likely, the $S = 6$ one cannot be ruled out.

From Figure 9 it could be argued that the $S = 3$ configuration should be assigned to the 1ML $\{Cr_{10}\}$/Au(111) sample, while that of $S = 6$ to the Cu(111) substrate. However, this assignment would be probably an overinterpretation of the results, as we must be aware of the limitation of the MC simulations: first, we must consider the simplification in the D_i single-ion anisotropy constants, and second, that the simulation curves shown in Figure 9b do not come out from an actual least-squares fit of the J_{ij}, but from a consistent set of these values starting from the bulk case.

The magnetization curve of the 14ML sample lays between those of the 1ML and bulk single crystals (Figure 8a), which suggests that the modification of the spin configuration may vary from one layer to another, approaching the bulk magnetic behavior as the number of layers increases. Since the XAS spectra with soft X-rays, as in the present measurements, will only probe a few nm of $\{Cr_{10}\}$ layers which would be separated by distances of not more of 1 nm, the derived $M(H)$ curve shows the magnetic behaviour of only the uppermost ≈6 layers. We have not attempted a simulation of these experimental results, since it would imply over parameterizing the model by introducing a distribution of spin configuration changes with the layer number.

4.2. Comparison with Literature Results

The extraordinary dependence of the magnetic properties of $\{Cr_{10}\}$ on structural changes imposed by accommodation to the surface demonstrated in this work is consistent with previous works reported in the literature. In fact, the early study of the family of Cr^{3+} wheels $[Cr_{10}(OR)_{20}(O_2CR')_{10}]$ in powder reported by Low et al.,[74] already revealed an extraordinary dependence of the magnetic behavior on the type of ligand, with some members of the family showing overall FM magnetic behavior and others presenting AF behavior. In recent years, H.W.L. Fraser et al.[91,92] studied the dependence of exchange coupling constants on structural changes in a large family of Cr^{3+}-Cr^{3+} dimers coordinated by di-alkoxo bridges using DFT calculations and $\chi T(T)$ data and carboxylate and diethanolamine ligands. In the latter case, it was shown that the use of carboxylate/alkoxide $[Cr^{III}(OR)_2(OCO)]$ bridging units with a peculiar orbital counter-complementarity effect favored FM coupling. This is precisely the type of heteroleptic bridging unit used in the $\{Cr_{10}\}$ wheels, combining two alkoxides (OMe) and one carboxylate (O_2CCMe_3), and thus the result provided a rationale for the FM interactions observed in this member of the $[Cr_{10}(OR)_{20}(O_2CR')_{10}]$ family. Moreover, the DFT calculations by Fraser et al.[91,92] predicted high sensitivity of the sign and magnitude of the coupling constant J on even tiny structural variations in the Cr–O–Cr angles. Very recently, we demonstrated that very small differences (<1°) between the Cr–O–Cr inner angles of bulk $\{Cr_{10}\}$ give rise to positive and negative exchange coupling constants within the molecular ring in such a way to produce a wheel's coupling scheme that is at the origin of the intermediate $S = 9$. In this respect, it is interesting to note that these molecular wheels crystallize with different unit cell according to the employed method, which can lead to slightly different Cr–O distances and Cr–O–Cr angles upon different crystallization conditions. For instance, when $\{Cr_{10}\}$ is recrystallized from toluene,[20] it yields the same space group ($P\bar{1}$), but slightly different unit cell than that found in the single crystals obtained from the solvothermal synthesis.[74] Slightly different inner and outer Cr–O–Cr angles are found when comparing the two $\{Cr_{10}\}$ crystal structures. Consequently, the structural parameters of the $\{Cr_{10}\}$ molecules, which are already very sensitive to the crystal packing, may be further stressed when deposited onto the substrate or in a thin-film.

Previous studies on $\{Cr_7Ni\}$ wheels as single-crystals and as sub-monolayer samples have shown changes in the values of the exchange coupling constants, but the spin coupling scheme along the wheel is preserved upon the deposition on metallic substrates.[68,69,70] For the Cr_7Ni-bu antiferromagnetically coupled wheel sublimated on Au(111), the total magnetic moment curves, $m_{tot}(H)$, of Cr^{3+} and Ni^{2+} measured at different temperatures on a 1ML sample were above those of a polycrystalline thin-film (a bulk sample used as reference), for both types of ions,[70] in contrast to our results on $\{Cr_{10}\}$. Those results were explained within a single ion spin Hamiltonian model, including the single-ion anisotropies (D_i), and two different coupling constants accounting for the J_{CrCr} and J_{CrNi} exchange interactions. The values of the AF coupling constants in the thin film ($J_{CrCr}/k_B = -8.47$ K, $J_{CrNi}/k_B = -9.81$ K, expressed as $\mathcal{H} = -2\sum J_{ij}S_iS_j$), were reduced by a 22% when the molecules were deposited as 1ML, whereas it was not necessary to change the values of the anisotropies ($D_{Cr}/k_B = -0.35$ K and $D_{Ni}/k_B = -4.06$ K) to fit the experimental results. The structure of the low-energy levels of the grafted rings was unaltered by the reduction of the J_{ij} values, and only a small compression of the energy spectrum was observed because of the reduced exchange interactions. Additionally, functionalization was studied in these Cr_7Ni rings; the Cr_7Ni-3tpc wheel showed a reduction by 15% of $J_{Cr\text{-}Cr}$ leaving the J_{CrNi} unchanged with respect to the pristine (unfunctionalized) Cr_7Ni-piv bulk compound,[69] whereas sublimation onto Au(111) produced a further reduction of the AF coupling constants, amounting $J_{CrCr}/k_B = -6.09$ K, $J_{CrNi}/k_B = -2.9$ K.[69] For Cr_7Ni wheels grafted to Au(111) through different functional ligands, the Ni dichroic signal was larger the stronger the ligand-substrate bonding, suggesting that the distortion of the wheel is

modulated by the strains due to ligands-substrate bond. In that work, DFT calculations were performed to estimate changes in the J_{ij} constants under possible ring distortions. For a dilation of 5% in the Cr–Cr(Ni) distance (within the possible range for an isolated molecule compared to a molecule in a molecular crystal), the calculated J_{CrCr} and J_{CrNi} exchange coupling constants were 29% (60%) smaller as compared to the coupling constants in the not-dilated structure. In addition, a parabolic function of the J_{CrCr} coupling as a function of the bond angles in the carboxylate and fluorine bridges was argued.

Like in the above examples, the magnetic properties of $\{Cr_{10}\}$ are modulated by wheel distortions produced in the layered configuration, modifying the Cr–Cr coupling constants. However, in contrast to the Cr_7Ni wheels, the deposition of $\{Cr_{10}\}$ on metallic surfaces induces an enhancement of the AF interactions involving flipping two of the exchange coupling constants from FM to AF, which produces a change in the total spin of the molecule ($S = 3$ or $S = 6$), with respect to the total spin observed in the molecules in the bulk ($S = 9$).

5. Conclusions

Large cluster $\{Cr_{10}\}$ wheels of formula $\{Cr_{10}(OMe)_{20}(O_2CCMe_3)_{10}\}$ were successfully deposited on Au(111) and Cu(111) substrates by direct sublimation in UHV. STM images show the self-assembly of the $\{Cr_{10}\}$ wheels into monolayers with hexagonal symmetry. XPS analysis demonstrates the integrity of the deposited molecules. $\{Cr_{10}\}$ represents the largest metal-organic cluster that has ever been sublimated.

From XNLD experiments it was proven that there is a small anisotropy of electronic origin at the Cr^{3+} ion with distorted octahedral oxygen coordination. The magnetic-field dependence of the magnetic moment measured by XMCD in 1ML samples on Au(111) and Cu(111) substrates is slightly different, showing the sensitivity of the magnetic properties of $\{Cr_{10}\}$ to structural changes imposed by surface deposition. Moreover, $m_{tot}(H)$ measured for 1ML samples is lower than that of a thin 14ML sample, which is in turn below that of the bulk compound. This result suggests that structural stress imposed by self-assembly onto the substrate relaxes in the successive layers. Thus, the magnetic properties of the multilayer samples progressively approach those of the bulk as coherence with the substrate is lost.

Monte Carlo calculations allowed us to rationalize the magnetic field dependence of the magnetization observed in the on-surface 1ML $\{Cr_{10}\}$ samples in terms of a change in the spin coupling configuration along the wheel, plausibly induced by on-surface deposition, changing the original total spin ground-state from $S = 9$ in the bulk compound to $S = 3$ or $S = 6$ in the molecules as 1ML samples. Despite the initial total spin of $\{Cr_{10}\}$ is reduced upon deposition, the array of self-assembled sublimated still supports a non-zero magnetic moment.

The above results emphasize the importance of characterizing the on-surface magnetic properties and spin ground-state of molecular nanomagnets, as they may be significantly different from those in the bulk, and from one cluster system to another. The present case shows a reduction of the molecules' ground-state total spin upon deposition, but other molecules might display an increase if the bulk exchange coupling constants are not very high. The capability of assembling 2D monolayers of $[Cr_{10}(OR)_{20}(O_2CR')_{10}]$ onto substrates opens an interesting playground to study, and eventually tune, the magnetic properties of cyclic clusters with non-zero spin for applications. The extreme sensitivity of the magnetic configuration to minor distortions of the intramolecular conformation might be exploited to control magnetism by external stimuli such as electric fields, pressure, solvents etc.

6. Experimental Section

$\{Cr_{10}(OMe)_{20}(O_2CCMe_3)_{10}\}$ single crystals were prepared by a solvothermal reaction using a method previously described,[20] starting from $\{[Cr_6F_7(O_2CCMe_3)_{10}][NH_2Et_3]_3\}_2$. The crystal structure was checked by X-ray diffraction and coincided with that earlier described.[74]

Initial deposition experiments were performed in an ultra-high vacuum (UHV) chamber (base pressure of 10^{-10} mbar), equipped with an Omicron VT Scanning Tunneling Microscope (STM), Low-Energy Electron Diffraction (LEED), and X-ray Photoelectron Spectroscopy (XPS) analysis tools at Padua University.

XPS measurements were performed with a Thermo Scientific ESCALAB QXi spectrometer employing a monochromatic Al Kα X-ray source (1486.6 eV) with a 650 μm × 200 μm spot size. For measurements of the bulk, a few mg of $\{Cr_{10}\}$ single crystals were mounted on double-side sticky carbon tape attached to the sample holder. The operating vacuum conditions of the analysis chamber were better than 10^{-8} mbar. Survey scans were measured in a binding energy range of 0–1350 eV using a constant pass energy of 200 eV at 1.0 eV/step. High-resolution spectra were recorded using a constant pass energy of 15 eV at 0.1 eV/step. The high-resolution XPS spectra were used for assessment of the elemental state as well as for quantification using the sensitivity factors provided by the Thermo Fischer Avantage software and after background correction the with smart-background function implemented in the same software. Fitting of C1s and O1s was performed with the Thermo Fischer Avantage software. The BE shifts were corrected by assigning to the C1s peak associated with aliphatic carbon a value of 284.8 eV.

During the synchrotron experiment, samples of $\{Cr_{10}\}$ were sublimated onto metallic substrates in a vacuum chamber in UHV conditions, similar to the setup used in Padua, and characterized in situ by STM to assess the formation of monolayers. The deposited samples, mounted on the STM plate, were then transported through a system of UHV tubes to the XAS-XMCD experimental chamber. This work reported results on three different samples: a monolayer sample on a polycrystalline Au(111)/mica substrate (denoted 1ML $\{Cr_{10}\}$/Au), a 14-layer sample deposited onto an Au(111) single crystal (denoted 14ML $\{Cr_{10}\}$/Au), and a monolayer deposited onto a Cu(111) single crystal (1ML $\{Cr_{10}\}$/Cu). The molecules were sublimated in UHV on the metal substrates from a PBN a crucible held at temperature of 250 °C.

Soft X-ray absorption and magnetic dichroism experiments at the Cr $L_{2,3}$ edge were carried out at the BL29 BOREAS beamline in ALBA synchrotron radiation facility, provided with a high-field vector magnet (HECTOR) end station. The sample was oriented with the substrate perpendicular to the synchrotron ring. Experiments were performed with the X-ray beam forming an angle between the beam direction and the direction normal to the plane varying between $\gamma = 0° - 70°$. The detection mode was total electron yield (TEY).

X-ray linear polarization absorption measurement were performed for a given incidence angle (γ), with the polarization of the electric field $\boldsymbol{E}$ parallel to the substrate (V), $\boldsymbol{E}_V$, or perpendicular to that direction (H), $\boldsymbol{E}_H$, see inset in Figure 4. In XMCD experiments the incoming light was right and left circularly polarized. XMCD spectra were measured at the maximum available magnetic field ($\mu_0 H = 6$ T). The temperature at the sample position was $T = 3.4 \pm 0.5$ K, as determined by calibration experiments at BOREAS.

In order to avoid sample degradation due to radiation exposure the beam front-end was closed between measurement runs; experiments were

done at very low flux ($<10^{12}$ photons/s), exposing fresh sample regions in every minimal XNLD or XMCD group of spectra, and XAS spectra were monitored to detect radiation damage. The XMCD spectra were determined from 2–4 XAS spectra with right- and left-handed circular polarizations. In addition, XMCD(H) cycles were performed by following the resonant L_3 peak intensity as a function of the magnetic field, while the magnetic field H was ramped at a rate of 2 T min^{-1} from 6 to −6 T and −6 to 6 T. The absolute XMCD scale was fixed at $\mu_0 H = 6$ T to the total magnetization moment value obtained from a full energy range XMCD scan.

To determine the {Cr_{10}} XAS signal of the molecular layer, the background contribution from the substrate had to be carefully subtracted. XAS, XMCD, and XNLD experiments on pristine Au and Cu substrates were performed under the same experimental conditions used for on-surface {Cr_{10}} samples. The background-subtracted XAS spectra were subsequently normalized to the atomic continuum signal at high energies.

Supporting Information

Supporting Information is available from the Wiley Online Library or from the author.

Acknowledgements

The authors acknowledge financial support from the Spanish Agencia Estatal de Investigación, through projects PID2020-115159GB-I00/AEI/10.13039/501100011033, Aragonese project RASMIA E12-23R co-funded by Fondo Social Europeo of the European Union FEDER (ES). Also University of Padova Grants P-DISC#09BIRD2019-UNIPD SMOW. The XMCD experiments were performed at the BOREAS beamline of the ALBA Synchrotron Light Facility with the collaboration of ALBA staff. XPS and depth profiling were performed with an ESCALAB QXi spectrometer funded by "Sviluppo delle infrastrutture e programma biennale degli interventi del Consiglio Nazionale delle Ricerche (2019)."

Conflict of Interest

The authors declare no conflict of interest.

Data Availability Statement

The data that support the findings of this study are available from the corresponding author upon reasonable request.

Keywords

chromium wheels, scanning tunneling microscopy, single-molecule magnets, sublimated clusters, surface molecular magnetism, X-ray magnetic circular dichroism

Received: February 17, 2023
Revised: May 9, 2023
Published online: June 22, 2023

[1] A. Cornia, D. R. Talham, M. Affronte, in *Molecular Magnetic Materials: Concepts and Applications* (Eds.: B. Sieklucka, D. Pinkowicz), Wiley-VCH Verlag GmbH & Co. KGaA, Weinheim, Germany **2017**.
[2] R. Sessoli, D. Gatteschi, A. Caneschi, M. A. Novak, *Nature* **1993**, *365*, 141.
[3] A. Caneschi, D. Gatteschi, R. Sessoli, A. L. Barra, L. C. Brunel, M. Guillot, *J. Am. Chem. Soc.* **1991**, *113*, 5873.
[4] J. R. Friedman, M. P. Sarachik, J. Tejada, R. Ziolo, *Phys. Rev. Lett.* **1996**, *76*, 3830.
[5] D. Shao, X.-Y. Wang, *Chin. J. Chem.* **2020**, *38*, 1005.
[6] N. Ishikawa, M. Sugita, T. Ishikawa, S. Y. Koshihara, Y. Kaizu, *J. Am. Chem. Soc.* **2003**, *125*, 8694.
[7] E. Bartolomé, A. Arauzo, J. Luzón, J. Bartolomé, F. Bartolomé, in *Handbook of Magnetic Materials* (Ed.: E. Brück) Elsevier, Amsterdam, Netherlands **2017**.
[8] Z. Zhu, C. Zhao, T. Feng, X. Liu, X. Ying, X.-L. Li, Y.-Q. Zhang, J. Tang, *J. Am. Chem. Soc.* **2021**, *143*, 10077.
[9] C. A. P. Goodwin, F. Ortu, D. Reta, N. F. Chilton, D. P. Mills, *Nature* **2017**, *548*, 439.
[10] F.-S. Guo, B. M. Day, Y.-C. Chen, M.-L. Tong, A. Mansikkamäki, R. A. Layfield, *Science* **2018**, *364*, 1400.
[11] A. Caneschi, D. Gatteschi, F. Totti, *Coord. Chem. Rev.* **2015**, *289*, 357.
[12] T. A. Jung, R. R. Schlittler, J. K. Gimzewski, *Nature* **1997**, *386*, 696.
[13] E. Bartolomé, J. Bartolomé, F. Sedona, J. Lobo-Checa, D. Forrer, J. Herrero-Albillos, M. Piantek, J. Herrero-Martin, D. Betto, E. Velez-Fort, L. Garcia, M. Panighel, A. Mugarza, M. Sambi, F. Bartolome, *J. Phys. Chem. C* **2020**, *124*, 13993.
[14] J. Otsuki, *Coord. Chem. Rev.* **2010**, *254*, 2311.
[15] H. Ma, L. Yang, N. Pan, S. Yau, J. Hang, K. Itaya, *Langmuir* **2006**, *22*, 2105.
[16] J. Gómez-Segura, I. Díez-Pérez, N. Ishikawa, M. Nakano, J. Veciana, D. Ruiz-Molina, *Chem. Commun.* **2006**, *27*, 2866.
[17] M. Mannini, F. Pineider, P. Sainctavit, C. Danieli, E. Otero, C. Sciancalepore, A. M. Talarico, M. Arrio, A. Cornia, D. Gatteschi, R. Sessoli, *Nat. Mater.* **2009**, *8*, 194.
[18] F. Moro, V. Corradini, M. Evangelisti, R. Biagi, V. De Renzi, U. del Pennino, J. C. Cezar, R. Inglis, C. J. Milios, E. K. Brechin, *Nanoscale* **2010**, *2*, 2698.
[19] A. Ghirri, V. Corradini, V. Bellini, R. Biagi, U. Del Pennino, V. De Renzi, J. C. Cezar, C. A. Muryn, G. A. Timco, R. E. P. Winpenny, M. Affronte, *ACS Nano* **2011**, *5*, 7090.
[20] M. Rancan, F. Sedona, M. Di Marino, L. Armelao, M. Sambi, *Chem. Commun. (Camb)* **2011**, *47*, 5744.
[21] L. Margheriti, M. Mannini, L. Sorace, L. Gorini, D. Gatteschi, A. Caneschi, D. Chiappe, R. Moroni, F. B. de Mongeot, A. Cornia, F. M. Piras, A. Magnani, R. Sessoli, *Small* **2009**, *5*, 1460.
[22] C. Wäckerlin, F. Donati, A. Singha, R. Baltic, S. Rusponi, K. Diller, F. Patthey, M. Pivetta, Y. Lan, S. Klyatskaya, M. Ruben, H. Brune, J. Dreiser, *Adv. Mater.* **2016**, *28*, 5195.
[23] G. Serrano, E. Velez-Fort, I. Cimatti, B. Cortigiani, L. Malavolti, D. Betto, A. Ouerghi, N. B. Brookes, M. Mannini, R. Sessoli, *Nanoscale* **2018**, *10*, 2715.
[24] L. Margheriti, D. Chiappe, M. Mannini, P. Car, P. Sainctavit, M.-A. Arrio, F. B. de Mongeot, J. C. Cezar, F. M. Piras, A. Magnani, E. Otero, A. Caneschi, *Adv. Mater.* **2010**, *22*, 5488.
[25] M. Mannini, F. Bertani, C. Tudisco, L. Malavolti, L. Poggini, K. Misztal, D. Menozzi, A. Motta, E. Otero, P. Ohresser, P. Sainctavit, G. G. Condorelli, E. Dalcanale, R. Sessoli, *Nat. Commun.* **2014**, *5*, 4582.
[26] A. Pedrini, L. Poggini, C. Tudisco, M. Torelli, A. E. Giuffrida, F. Bertani, I. Cimatti, E. Otero, P. Ohresser, P. Sainctavit, M. Suman, G. G. Condorelli, M. Mannini, E. Dalcanale, *Small* **2018**, *14*, 1702572.
[27] D. Moreno, S. O. Parreiras, J. I. Urgel, B. Muñiz-Cano, C. Martín-Fuentes, K. Lauwaet, M. Valvidares, M. A. Valbuena, J. M. Gallego, J. I. Martínez, P. Gargiani, J. Camarero, R. Miranda, D. Écija, *Small* **2022**, *18*, 2107073.
[28] A. Popov, S. Yang, L. Dunsch, *Chem. Rev.* **2013**, *113*, 5989.

[29] E. Koutsouflakis, D. Krylov, N. Bachellier, D. Sostina, V. Dubrovin, F. Liu, L. Spree, G. Velkos, S. Schimmel, Y. Wang, *Nanoscale* **2022**, *14*, 9877.
[30] D. D. S. Krylov, S. Schimmel, V. Dubrovin, D. F. Liu, T. T. N. Nguyen, L. Spree, P. C.-H. Chen, G. Velkos, C. Bulbucan, R. Westerström, M. Studniarek, J. Dreiser, C. Hess, B. Büchner, S. M. Avdoshenko, A. A. Popov, *Angew. Chem., Int. Ed.* **2020**, *59*, 5756.
[31] L. Spree, F. Liu, V. Neu, M. Rosenkranz, G. Velkos, Y. Wang, S. Schiemenz, J. Dreiser, P. Gargiani, M. Valvidares, C.-H. Chen, B. Büchner, S. M. Avdoshenko, A. A. Popov, *Adv. Funct. Mater.* **2021**, *31*, 2105516.
[32] M. Mannini, P. Sainctavit, R. Sessoli, C. C. dit Moulin, F. Pineider, M.-A. Arrio, A. Cornia, D. Gatteschi, *Phys. Chem. Glasses: Eur. J. Glass Sci. Technol., Part B* **2008**, *14*, 7530.
[33] M. Mannini, F. Pineider, P. Sainctavit, L. Joly, A. Fraile-Rodriguez, M. Arrio, C. Moulin, W. Wernsdorfer, A. Cornia, *Adv. Mater.* **2009**, *21*, 167.
[34] M. Mannini, F. Pineider, P. Sainctavit, C. Danieli, E. Otero, C. Sciancalepore, A. M. Talarico, M.-A. Arrio, A. Cornia, D. Gatteschi, S. Roberta, *Nat. Mater.* **2009**, *8*, 194.
[35] L. Malavolti, V. Lanzilotto, S. Ninova, L. Poggini, I. Cimatti, B. Cortigiani, L. Margheriti, D. Chiappe, E. Otero, P. Sainctavit, F. Totti, A. Cornia, M. Mannini, R. Sessoli, *Nano Lett.* **2015**, *15*, 535.
[36] G. Serrano, L. Poggini, M. Briganti, A. L. Sorrentino, G. Cucinotta, L. Malavolti, B. Cortigiani, E. Otero, P. Sainctavit, S. Loth, F. Parenti, A.-L. Barra, A. Vindigni, A. Cornia, F. Totti, M. Mannini, R. Sessoli, *Nat. Mater. 19*, 546.
[37] A. Cornia, M. Mannini, R. Sessoli, D. Gatteschi, *Eur. J. Inorg. Chem.* **2019**, *2019*, 552.
[38] M. Mannini, F. Pineider, C. Danieli, F. Totti, L. Sorace, P. Sainctavit, M. Arrio, E. Otero, L. Joly, J. C. Cezar, a. Cornia, R. Sessoli, *Nature* **2010**, *468*, 417.
[39] V. Corradini, A. Ghirri, U. del Pennino, R. Biagi, V. A. Milway, G. Timco, F. Tuna, R. E. P. Winpenny, M. Affronte, *Dalton Trans.* **2010**, *39*, 4928.
[40] F. Meier, J. Levy, D. Loss, *Phys. Rev. Lett.* **2003**, *90*, 047901.
[41] F. Troiani, A. Ghirri, M. Affronte, S. Carretta, P. Santini, G. Amoretti, S. Piligkos, G. Timco, R. E. P. Winpenny, *Phys. Rev. Lett.* **2005**, *94*, 207208.
[42] A. Ghirri, F. Troiani, M. Affronte, in *Molecular Nanomagnets and Related Phenomena*, Springer, Berlin **2015**.
[43] G. L. Abbati, A. Cornia, A. C. Fabretti, A. Caneschi, D. Gatteschi, *Inorg. Chem.* **1998**, *37*, 1430.
[44] A. J. Blake, C. M. Grant, S. Parsons, J. M. Rawson, *J. Chem. Soc. Chem. Commun.* **1994**, *20*, 2364.
[45] R. W. Saalfrank, I. Bernt, M. M. Chowdhry, F. Hampel, G. B. M. Vaughan, **2001**, *7*, 2765.
[46] D. Gatteschi, A. Caneschi, L. Pardi, R. Sessoli, *Science (80-.)* **1994**, *265*, 1054.
[47] B. Normand, X. Wang, X. Zotos, D. Loss, *Phys. Rev. B* **2001**, *63*, 184409.
[48] K. L. Taft, C. D. Delfs, G. C. Papaefthymiou, S. Foner, D. Gatteschi, S. J. Lippard, *J. Am. Chem. Soc.* **1994**, *114*, 823.
[49] C. P. Raptopoulou, V. Tangoulis, E. Devlin, *Angew. Chem., Int. Ed.* **2002**, *41*, 2386.
[50] J. Ummethum, J. Nehrkorn, S. Mukherjee, N. B. Ivanov, S. Stuiber, T. Strässle, P. L. W. Tregenna-Piggott, H. Mutka, G. Christou, O. Waldmann, J. Schnack, *Phys. Rev. B* **2012**, *86*, 104403.
[51] v. S. Joris, R. Sessoli, D. Gatteschi, A. A. Smith, M. Helliwell, R. E. P. Winpenny, A. Cornia, A. Barra, A. G. M. Jansen, E. Rentschler, G. A. Timco, *Chem. -Eur. J* **2002**, *8*, 277.
[52] S. Carretta, J. v. Slageren, T. Guidi, E. Liviotti, C. Mondelli, D. Rovai, A. Cornia, A. L. Dearden, F. Carsughi, M. Affronte, C. D. Frost, R. E. P. Winpenny, D. Gatteschi, G. Amoretti, R. Caciuffo, *Phys. Rev. B* **2003**, *67*, 094405.
[53] M. L. Baker, T. Guidi, S. Carretta, J. Ollivier, H. Mutka, H. U. Gudel, G. A. Timco, E. J. L. McInnes, G. Amoretti, R. E. P. Winpenny, P. Santini, *Nat. Phys.* **2012**, *8*, 906.
[54] A. Chiolero, D. Loss, *Phys. Rev. Lett.* **1998**, *80*, 169.
[55] M. Affronte, A. Ghirri, S. Carretta, G. Amoretti, S. Piligkos, G. Timco, R. Winpenny, *Appl. Phys. Lett.* **2004**, *84*, 3468.
[56] E. Garlatti, S. Bordignon, S. Carretta, G. Allodi, G. Amoretti, R. D.e Renzi, A. Lascialfari, Y. Furukawa, G. A. Timco, R. Woolfson, R. E. P. Winpenny, P. Santini, *Phys. Rev. B* **2016**, *93*, 024424.
[57] E. J. L. McInnes, S. Piligkos, G. A. Timco, R. E. P. Winpenny, *Coord. Chem. Rev.* **2005**, *249*, 2577.
[58] M. Affronte, S. Carretta, G. A. Timco, R. E. P. A. R. C. Winpenny, *Chem* **2007**, *18*, 1789.
[59] E. McInnes, G. A. Timco, G. F. S. Whitehead, R. E. P. Winpenny, *Angew. Chem., Int. Ed.* **2015**, *54*, 14244.
[60] E. Garlatti, M. A. Albring, M. L. Baker, R. J. Docherty, H. Mutka, T. Guidi, V. G. Sakai, G. F. S. Whitehead, R. G. Pritchard, G. A. Timco, F. Tuna, G. Amoretti, S. Carretta, P. Santini, G. Lorusso, M. Affronte, E. J. L. McInnes, D. Collison, R. E. P. Winpenny, *J. Am. Chem. Soc.* **2014**, *136*, 9763.
[61] E. Garlatti, T. Guidi, A. Chiesa, S. Ansbro, M. L. Baker, J. Ollivier, H. Mutka, G. A. Timco, I. Vitorica-Yrezabal, E. Pavarini, P. Santini, G. Amoretti, R. E. P. Winpenny, S. Carretta, *Chem. Sci.* **2018**, *9*, 3555.
[62] S. Carretta, P. Santini, G. Amoretti, M. Affronte, A. Ghirri, I. Sheikin, S. Piligkos, G. Timco, R. E. P. Winpenny, *Phys Rev B* **2005**, *72*, 060403.
[63] S. Carretta, P. Santini, G. Amoretti, T. Guidi, J. R. D. Copley, Y. Qiu, R. Caciuffo, G. Timco, R. E. P. Winpenny, *Phys. Rev. Lett.* **2007**, *98*, 167401.
[64] F. Adelnia, L. Bordonali, M. Mariani, S. Bordignon, G. Timco, R. Winpenny, F. Borsa, A. Lascialfari, *J. Phys. Condens. Matter* **2015**, *27*, 506001.
[65] T. Guidi, B. Gillon, S. A. Mason, E. Garlatti, S. Carretta, P. Santini, A. Stunault, R. Caciuffo, J. v. Slageren, B. Klemke, A. Cousson, G. A. Timco, R. E. P. Winpenny, *Nat. Commun.* **2015**, *6*, 7061.
[66] E. Garlatti, G. Allodi, S. Bordignon, L. Bordonali, G. A. Timco, R. E. P. Winpenny, A. Lascialfari, R. De Renzi, S. Carretta, *J. Phys. Condens. Matter* **2020**, *32*, 244003.
[67] F. K. Larsen, E. J. L. McInnes, H. E.l Mkami, J. Overgaard, S. Piligkos, G. Rajaraman, E. Rentschler, A. A. Smith, G. M. Smith, V. Boote, M. Jennings, G. A. Timco, R. E. P. Winpenny, *Angew. Chem., Int. Ed.* **2003**, *42*, 101.
[68] V. Corradini, F. Moro, R. Biagi, U. Del Pennino, V. De Renzi, S. Carretta, P. Santini, M. Affronte, J. C. Cezar, G. Timco, R. E. P. Winpenny, *Phys. Rev. B* **2008**, *77*, 014402.
[69] V. Corradini, F. Moro, R. Biagi, V. De Renzi, U. del Pennino, V. Bellini, S. Carreta, P. Santini, V. A. Milway, R. E. P. Winpenny, M. Affronte, *Phys. Rev. B* **2009**, *79*, 144419.
[70] V. Corradini, A. Ghirri, E. Garlatti, R. Biagi, V. De Renzi, U. del Pennino, V. Bellini, S. Carretta, P. Santini, G. Timco, R. E. P. Winpenny, M. Affronte, *Adv. Funct. Mater.* **2012**, *22*, 3706.
[71] G. Lorusso, V. Corradini, A. Ghirri, R. Biagi, U. Del Pennino, I. Siloi, F. Troiani, G. Timco, R. E. P. Winpenny, M. Affronte, *Phys. Rev. B* **2012**, *86*, 184424.
[72] S. Carretta, J. van Slageren, T. Guidi, E. Liviotti, C. Mondelli, D. Rovai, A. Cornia, A. L. Dearden, F. Carsughi, M. Affronte, C. D. Frost, R. E. P. Winpenny, D. Gatteschi, G. Amoretti, R. Caciuffo, *Phys. Rev. B.* **2003**, *67*, 094405.
[73] A. L. Dearden, S. Parsons, R. E. P. Winpenny, *Angew. Chem.* **2001**, *113*, 155.
[74] D. M. Low, G. Rajaraman, M. Helliwell, G. Timco, J. Van Slageren, R. Sessoli, S. T. Ochsenbein, R. Bircher, C. Dobe, O. Waldmann, H. U. Güdel, M. a. Adams, E. Ruiz, S. Alvarez, E. J. L. McInnes, *Chem. –Eur. J.* **2006**, *12*, 1385.

[75] S. Sharmin, A. Ardavan, S. J. Blundell, A. I. Coldea, E. J. L. Low, D. McInnes, *Appl. Phys. Lett.* **2015**, *86*, 032507.
[76] J. Rubín, A. Arauzo, E. Bartolomé, F. Sedona, M. Rancan, L. Armelao, J. Luzón, T. Guidi, E. Garlatti, F. Wilhelm, A. Rogalev, A. Amann, S. Spagna, J. Bartolomé, F. Bartolomé, *J. Am. Chem. Soc.* **2022**, *144*, 12520.
[77] S. T. Ochsenbein, F. Tuna, M. Rancan, R. S. G. Davies, C. A. Muryn, O. Waldmann, R. Bircher, A. Sieber, G. Carver, H. Mutka, F. Fernandez-Alonso, A. Podlesnyak, L. P. Engelhardt, G. A. Timco, H. U. Gudel, *Chem. -Eur. J.* **2008**, *14*, 5144.
[78] D. S. M. D. S. Clure, D. S. Mc Clure, *Sol. Syst. Plasma Phys.* **1959**, *9*, 399.
[79] M. Llunell, D. Casanova, J. Cirera, P. Alemany, S. Alvarez, SHAPE User's Manual. Version 2.1 **2013**, https://cosymlib.readthedocs.io/en/latest/_downloads/50808a3dee9c2eb6b21cb1e3d1880765/manual_shape_2_1.pdf.
[80] J. P. Crocombette, B. T. Thole, F. Jollet, *J. Phys. Condens. Matter* **1996**, *8*, 4095.
[81] E. Goering, *Philos. Mag.* **2005**, *85*, 2895.
[82] A. Ghirri, G. Lorusso, F. Moro, F. Troiani, V. Corradini, C. Muryn, F. Tuna, G. Timco, R. E. P. Winpenny, M. Affronte, *Phys. Rev. B* **2009**, *79*, 224430.
[83] J. Stöhr, H. König, *Phys. Rev. Lett.* **1995**, *75*, 3748.
[84] J. Bartolomé, F. Bartolomé, L. M. García, G. Filoti, T. Gredig, C. N. Colesniuc, I. K. Schuller, J. C. Cezar, *Phys. Rev. B: Condens. Matter Mater. Phys.* **2010**, *81*, 195405.
[85] H. W. L. Fraser, L. Smythe, S. Dey, G. S. Nichol, S. Piligkos, G. Rajaraman, E. K. Brechin, *Dalton Trans.* **2018**, *47*, 8100.
[86] S. B. Darling, A. W. Rosenbaum, Y. Wang, S. J. Sibener, *Langmuir* **2002**, *18*, 7462.
[87] T. Duguet, E. Gaudry, T. Deniozou, J. Ledieu, M. C. de Weerd, T. Belmonte, J. M. Dubois, V. Fournée, *Phys. Rev. B* **2009**, *80*, 205412.
[88] D. Bencini, A. Gatteschi, *Electron Paramagentic Resonance of Exchange Coupled Systems*, Springer-Verlag, Berlin, Heidelberg **1990**.
[89] B. Bauer, L. D. Carr, H. G. Evertz, A. Feiguin, J. Freire, S. Fuchs, L. Gamper, J. Gukelberger, E. Gull, S. Guertler, A. Hehn, R. Igarashi, S. V. Isakov, D. Koop, P. N. Ma, P. Mates, H. Matsuo, O. Parcollet, G. Pawłowski, J. D. Picon, L. Pollet, E. Santos, V. W. Scarola, U. Schollwöck, C. Silva, B. Surer, S. Todo, S. Trebst, M. Troyer, M. L. Wall, et al., *J. Stat. Mech.* **2011**, *310*, P05001.
[90] A. F. Albuquerque, F. Alet, P. Corboz, P. Dayala, A. Feiguin, S. Fuchs, L. Gamper, E. Gull, S. Gürtlerf, A. Honecker, R. Igarashi, M. Körner, A. Kozhevnikov, A. Läuchli, S. R. Manmanak, M. Matsumoto, I. P. McCulloch, F. Michel, R. M. Noack, G. L. P. Pawłowski, *J. Magn. Magn. Mater.* **2007**, *310*, 1187.
[91] H. Fraser, G. S. Nichol, G. Velmuragan, G. Rajaraman, E. K. Brechin, *Dalton Trans.* **2017**, *46*, 7159.
[92] H. Fraser, L. Smythe, S. Dey, G. Nichol, S. Piligkos, G. Rajaraman, E. Brechin, *Dalton Trans.* **2018**, *47*, 8100.